Magnetic Resonance Elastography Reconstruction for Anisotropic Tissues

Behzad Babaei, Daniel Fovargue, Robert A Lloyd, Renee Miller, Lauriane Jugé, Max Kaplan, David A Nordsletten, Ralph Sinkus, Lynne E Bilston

To cite this version:

Behzad Babaei, Daniel Fovargue, Robert A Lloyd, Renee Miller, Lauriane Jugé, et al.. Magnetic Resonance Elastography Reconstruction for Anisotropic Tissues. Medical Image Analysis, 2021, 74, pp.102212. 10.1016/j.media.2021.102212 . hal-03409061

HAL Id: hal-03409061
https://hal.science/hal-03409061v1

Medical Image Analysis 74 (2021) 102212

Contents lists available at ScienceDirect

Medical Image Analysis

journal homepage: www.elsevier.com/locate/media

Magnetic Resonance Elastography Reconstruction for Anisotropic Tissues

Behzad Babaei[a,f,1], Daniel Fovargue[c,1], Robert A. Lloyd[a,b,1], Renee Miller[c,1], Lauriane Jugé[g], Max Kaplan[a,e], Ralph Sinkus[c], David A. Nordsletten[c,d,2], Lynne E. Bilston[a,b,2,*]

[a] *Neuroscience Research Australia, Sydney, NSW, Australia*
[b] *Prince of Wales Clinical School, University of New South Wales, Sydney, NSW, Australia*
[c] *School of Biomedical Engineering and Imaging Sciences, The Rayne Institute, King's College London, SE1 7EH, London, United Kingdom*
[d] *Department of Surgery and Biomedical Engineering, University of Michigan, Ann Arbor, MI, United States of America*
[e] *Graduate School of Biomedical Engineering, University of New South Wales, Sydney, NSW, Australia*
[f] *School of Mechanical and Manufacturing Engineering, University of New South Wales, Sydney, NSW, Australia*
[g] *School of Medical Sciences, University of New South Wales, Sydney, NSW, Australia*

ARTICLE INFO

Article history:
Received 25 January 2021
Revised 2 June 2021
Accepted 4 August 2021
Available online 20 September 2021

Keywords:
Magnetic Resonance Elastography
Elastography reconstruction
Anisotropic reconstruction
biomechanics
linear viscoelastic wave equations

ABSTRACT

Elastography has become widely used clinically for characterising changes in soft tissue mechanics that are associated with altered tissue structure and composition. However, some soft tissues, such as muscle, are not isotropic as is assumed in clinical elastography implementations. This limits the ability of these methods to capture changes in anisotropic tissues associated with disease. The objective of this study was to develop and validate a novel elastography reconstruction technique suitable for estimating the linear viscoelastic mechanical properties of transversely isotropic soft tissues. We derived a divergence-free formulation of the governing equations for acoustic wave propagation through a linearly transversely isotropic viscoelastic material, and transformed this into a weak form. This was then implemented into a finite element framework, enabling the analysis of wave input data and tissue structural fibre orientations, in this case based on diffusion tensor imaging. To validate the material constants obtained with this method, numerous *in silico* phantom experiments were run which encompassed a range of variations in wave input directions, material properties, fibre structure and noise. The method was also tested on *ex vivo* muscle and *in vivo* human volunteer calf muscles, and compared with a previous curl-based inversion method. The new method robustly extracted the transversely isotropic shear moduli ($G'_{\perp}$, $G'_{\parallel}$, G'') from the *in silico* phantom tests with minimal bias, including in the presence of experimentally realistic levels of noise in either fibre orientation or wave data. This new method performed better than the previous method in the presence of noise. Anisotropy estimates from the *ex vivo* muscle phantom agreed well with rheological tests. *In vivo* experiments on human calf muscles were able to detect increases in muscle shear moduli with passive muscle stretch. This new reconstruction method can be applied to quantify tissue mechanical properties of anisotropic soft tissues, such as muscle, in health and disease.

1. Introduction

Tissue mechanical properties have long been linked to tissue structure and function (Bayly et al., 2014; Geng et al., 2009; Llinares-Benadero and Borrell, 2019). Consequently, changes in tissue mechanical behaviour are often associated with a broad range of clinical pathologies, such as tumours and neuromuscular disorders, which alter tissue composition and structure. More recently, tissue stiffness has also been used as a surrogate marker of disease progression and/or treatment response. In some cancers, increased peri-tumoural stiffness has been shown to facilitate metastasis (Chaudhuri et al., 2018; Gkretsi and Stylianopoulos, 2018; Novak et al., 2018). Studies of an animal model of muscular dystrophy (Qin et al., 2014), the tongues of sleep apnoeics (Brown et al., 2014), and the thigh muscle of hyperthyroid patients have shown that disease-related changes in mus-

---

[*] Corresponding author.
E-mail address: l.bilston@neura.edu.au (L.E. Bilston).
[1] These authors contributed equally as first authors and are listed in alphabetical order by last name.
[2] These authors contributed equally as senior authors.

https://doi.org/10.1016/j.media.2021.102212

cle anisotropy can be detected (Bensamoun et al., 2007). Historically, changes in the mechanical properties of superficial tissues have been identified by palpation. However, quantitative methods of characterising tissue stiffness in disease states have become an active area of research in recent years, in part, due to technical developments enabling non-invasive measurements such as elastography.

Elastography relies on the knowledge that the speed and attenuation of small amplitude waves travelling through a medium are directly related to the mechanical properties of the material. Elastography techniques involve (a) inducing a mechanical or acoustic wave which propagates through the tissue, (b) measuring the resulting harmonic wave displacements and (c) using a reconstruction method to relate the wave displacements to the material's mechanical properties. In soft tissue applications, ultrasound (Gennisson et al., 2013; Sigrist et al., 2017), optical (Wang and Larin, 2015) and magnetic resonance (MR) (Muthupillai et al., 1995; Sinkus et al., 2000) imaging modalities for elastography have been developed. Some ultrasound-based techniques use time-of-flight to estimate wave speed and thus elasticity, but newer ultrasound approaches and MR elastography most commonly use a sinusoidal steady-state vibration input that is imaged synchronously over the domain of interest. This time-varying displacement data is then used to estimate tissue mechanical properties, typically quantified by the shear modulus. Of particular interest here, MR elastography (MRE) most commonly delivers external vibration to the tissue using a transducer that is synchronised to the imaging sequence. Motion-sensitive gradients are added to the imaging sequence such that the displacements are encoded in the phase images at several time points across each vibration cycle (Muthupillai et al., 1995; Sinkus et al., 2000).

MRE has had its widest clinical usage to date in quantifying the mechanical properties of liver tissue, particularly in disorders involving fibrotic changes. These applications assume that the tissue is isotropic, and are based around solving the isotropic linear viscoelastic wave equation. However, assumptions of isotropy break down in tissues such as skeletal muscle, heart muscle and potentially also white matter in the central nervous system. Anisotropy of passive muscle tissue is well established, both from *ex vivo* (Takaza et al., 2013; Tan et al., 2015) and a limited number of *in vivo* studies (Gennisson et al., 2010). Some of the issues associated with using an isotropic reconstruction method on anisotropic tissues are reviewed in Bilston (2018); Bilston et al. (2019); Bilston and Tan (2014). Anisotropy in neural tissue is less well-established, with substantial variation and inconsistent results, both in tissue rheology experiments (see Bilston (2019); Cheng et al. (2008); Feng et al. (2013) for reviews) and *in vivo* MRE (Green et al., 0000; Romano et al., 2012; Anderson et al., 2016; Kalra et al., 2019). Neglecting the anisotropy of such tissues can lead to inaccurate estimates of mechanical properties, and likely also reduces the sensitivity of MRE to detect changes that affect only one structural direction, such as degenerative muscle disorders (Qin et al., 2014). Introduction of deformation, either through compression in disease (Fovargue et al., 2020), or due to physiological loading (Capilnasiu et al., 2019) has also been shown to introduce apparent anisotropy due to local material tension and compression.

In MRE, there have been several attempts to develop methods for estimating anisotropic tissue properties. Most of these studies assume that the tissue is transversely isotropic, adopting various strategies to estimate the shear modulus along the local axis of symmetry (fibre direction) and perpendicular to it. These methods vary considerably in approach and complexity. The theory of elastic solids requires five parameters to fully describe the behaviour of a transversely isotropic material. Numerous MRE studies make an assumption of incompressibility, thus reducing the number of independent parameters to three, which typically include two shear parameters, describing shear behaviour parallel and perpendicular to the axis of symmetry, as well as a parameter describing the tensile behaviour (e.g. Guo et al. (2015); Tweten et al. (2015)). Additional studies have simplified the material description further to include only two shear parameters (Sinkus et al., 2005), motivated by the fact that the nearly incompressible nature of tissue leads to a much higher compressional wave speed compared to the shear wave speeds.

Aside from the choice of independent parameters, each method utilises different methods for parameter reconstruction. One approach estimates tissue properties based on measuring the wavelength of shear waves propagating in different directions (Bensamoun et al., 2008). However, this technique is prone to bias except in geometrically simple systems with controllable wave inputs (Namani et al., 2009). A related class of methods uses different filters to extract waves propagating in the direction of fibres (often called 'waveguides'), and then estimates anisotropic parameters (Romano et al., 2012; Kalra et al., 2019). These methods limit tissue property estimation to these identified waveguide regions. Further methods have used vector projection onto specific polarization directions to decompose the complex displacements into slow and fast shear waves (Tweten et al., 2015; 2017; Schmidt et al., 2018; Smith et al., 2020). These methods suffer when waves propagate in a single direction (Tweten et al., 2017). Filtering methods typically utilise either local frequency estimation (LFE) (Knutsson et al., 1994) or direct inversion (DI) (Okamoto et al., 2011) to reconstruct stiffness along given directions.

Sinkus et al. (2005) estimated anisotropic properties of breast tissue by numerically solving the transversely isotropic linear viscoelastic wave equation, using a finite difference scheme and optimisation to identify the symmetry directions. This method, while comprehensive, requires extremely high-quality data, is computationally intensive, assumes commutative properties of the microstructural variations and has not been experimentally validated. An extension of this approach identifies the axis of structural symmetry in the tissue using diffusion tensor imaging (DTI), and uses these directions along with 3D wave image data to solve the full anisotropic wave equation. The latter method, combining MRE and DTI data, has been partially validated *in silico* and *ex vivo*, and applied *in vivo* in both human and animal studies (Brown et al., 2014; Cheng et al., 2011; Green et al., 2013; Qin et al., 2013a; 2014). While showing promise, this approach requires high quality wave and DTI data in matching coordinates since any distortion in DTI data due to EPI artefacts can lead to mismatch between the MRE and DTI data. From this brief summary, it is clear that there is a need for a validated and more numerically robust approach for estimating tissue anisotropy from MR elastography, which bypasses the need for directional filtering, is less sensitive to noisy data and can be universally and rapidly employed with *in vivo* MRE and DTI data.

In this paper, we present a novel method of anisotropic MRE reconstruction based on a finite element inversion. This approach extends our recent isotropic finite element inversion method (Fovargue et al., 2018a; 2018b) to transversely isotropic tissues. Importantly, in our approach, commutative assumptions about the variation of fibre directions are circumvented. This technique is adapted to enable use of multiple wave image sets in order to improve robustness and accuracy of results. The reconstruction technique is validated using an extensive array of anisotropic *in silico* phantom datasets that explore the technique's sensitivity to stiffness, fibre variations, noise (in displacements and fibre orientations), viscosity and loading conditions. The technique is also tested on *ex vivo* muscle tissue and results are compared to rheometry. The method is then used *in vivo*, by measuring anisotropic muscle properties of the human calf muscles under different degrees of passive stretch. To achieve the latter, we combine the MRE inversion with an image processing and registration pipeline that co-registers the MRE and DTI data, and uses tractography to identify the muscle fibre orientations at each pixel.

In this paper, we introduce the basic assumptions for transversely isotropic materials, extend our divergence-free FEM inversion to these materials, and introduce data sources (section 2). The performance of the reconstruction is then analysed in *in silico, ex vivo* and *in vivo* datasets in section 3. Finally, the broader implication of these results for applications in clinical patients and research are discussed (section 4).

2. Methods

2.1. Wave motion through transversely isotropic materials

In magnetic resonance elastography, small amplitude harmonic waves (with angular velocity ω) are transmitted through the body or region of interest, $\Omega \subset \mathbb{R}^3$ (with boundary $\Gamma = \Gamma_D \cup \Gamma_N$). Under these conditions, the physical motion of the waves is typically considered to be governed by the linear viscoelastic wave equations (Fovargue et al., 2018b) shown in Eqs. 1-4. Under the time harmonic assumption, the displacement ($\mathbf{u} : \Omega \to \mathbb{C}^3$), hydrostatic stress ($p : \Omega \to \mathbb{C}$) and distortional Cauchy stress ($\boldsymbol{\sigma} : \Omega \to \mathbb{C}^{3\times3}$) are complex-valued functions of space. Each of these terms can be related to their physical time-dependent real-valued functions (denoted with a subscript r), *e.g.* $\mathbf{u}_r(\mathbf{x}, t) = \mathrm{Re}\{\mathbf{u}(\mathbf{x}) \exp(i\omega t)\}$.[3]

$$\rho\omega^2 \mathbf{u} + \nabla \cdot \boldsymbol{\sigma} + \nabla p = \mathbf{0}, \quad \text{on } \Omega \tag{1}$$

$$\nabla \cdot \mathbf{u} - \frac{p}{K} = 0, \quad \text{on } \Omega \tag{2}$$

$$\mathbf{u} = \hat{\mathbf{u}}, \qquad \Gamma_D \tag{3}$$

$$\boldsymbol{\sigma} \cdot \mathbf{n} = \hat{\mathbf{t}}, \qquad \Gamma_N \tag{4}$$

Within Eqs. 1 and 2, $\rho(\mathbf{x})$ denotes the material density and K is the complex bulk modulus of the material. Eqs. 3 and 4 reference the boundary conditions where known displacements $\hat{\mathbf{u}}$ or known tractions $\hat{\mathbf{t}}$ are applied over Γ_D and Γ_N, respectively. The distortional Cauchy stress, $\boldsymbol{\sigma} = \boldsymbol{\sigma}(\boldsymbol{\varepsilon})$, denotes the non-hydrostatic components of stress and is assumed to be a function of the small strain tensor $\boldsymbol{\varepsilon} = \frac{1}{2}(\nabla\mathbf{u} + \nabla\mathbf{u}^T)$. Importantly, $\boldsymbol{\sigma}$ is also dependent on material stiffness parameters which vary in number depending on the assumed form of the constitutive model. The linear viscoelastic wave equations above represent the nearly incompressible form (when $K < \infty$) and the incompressible form (when $K = \infty$), both of which are commonly employed (Romano et al., 1998; Van Houten et al., 2001; Connesson et al., 2015; Fovargue et al., 2018b). In the nearly incompressible case, the pressure can be statically condensed and eliminated from the system through substitution using Eq. (2), giving the common compressible form.

2.1.1. Isotropic and transversely isotropic material response

While Eqs. 1-4 are typically used to solve a forward problem, where all material parameters are given, in MRE material displacements, $\mathbf{u}$, is given with the material stiffness parameters being the primary unknowns requiring some inverse estimation. Various techniques are applied to eliminate hydrostatic effects and hence the impact of the bulk modulus, K. Making the common assumption of constant density ($\rho = 1000\ kg/m^3$), the only remaining free parameter(s) to ensure equality (or near equality) in Eq. (1) are the material stiffness parameters that are integrated within the definition of the distortional Cauchy stress. For the case of linearly viscoelastic isotropic materials, the real-valued distortional Cauchy stress is given by

$$\boldsymbol{\sigma}_r(\boldsymbol{\varepsilon}_r) = 2\mu\boldsymbol{\varepsilon}_r + 2\eta\dot{\boldsymbol{\varepsilon}}_r, \quad \sigma_{r,ij} = \left(\mu + \eta\frac{\partial}{\partial t}\right)\left(\frac{\partial u_{r,i}}{\partial x_j} + \frac{\partial u_{r,j}}{\partial x_i}\right), \tag{5}$$

or by the complex counterpart

$$\boldsymbol{\sigma}(\boldsymbol{\varepsilon}) = 2G\boldsymbol{\varepsilon}, \quad \sigma_{ij} = G\left(\frac{\partial u_i}{\partial x_j} + \frac{\partial u_j}{\partial x_i}\right),$$

with $G = G' + iG''$ denoting the shear modulus relating to the Lamé parameters, *e.g.* $G = \mu + i\omega\eta$. We note here that use of other viscoelastic forms, such as fractional linear viscoelasticity, changes the form of $\boldsymbol{\sigma}_r$. However, the complex counterpart $\boldsymbol{\sigma}$ remains the same, with a varying relationship between the shear modulus, G, and the Lamé parameters.

The isotropic formulation has been applied across a range of tissues (Fovargue et al., 2018b), and is by far the most commonly employed material model in MRE analysis. However, as noted, many tissues are known to exhibit anisotropic material response. The generalised extension to anisotropy for a linearly viscoelastic material extends the definition of Eq. (5) to account for all possible anisotropic responses (Malvern, 1969), *e.g.*

$$\boldsymbol{\sigma}_r(\boldsymbol{\varepsilon}_r) = 2\mathcal{C} : \boldsymbol{\varepsilon}_r + 2\mathcal{N} : \dot{\boldsymbol{\varepsilon}}, \quad \sigma_{r,ij} = 2\left(\mathcal{C}_{ijkl} + \mathcal{N}_{ijkl}\frac{\partial}{\partial t}\right)\varepsilon_{r,kl}. \tag{6}$$

with the complex counterpart (with $\mathcal{G} = \mathcal{C} + i\omega\mathcal{N}$),

$$\boldsymbol{\sigma}(\boldsymbol{\varepsilon}) = 2\mathcal{G} : \boldsymbol{\varepsilon}, \quad \sigma_{r,ij} = 2\mathcal{G}_{ijkl}\varepsilon_{kl}.$$

Here $\mathcal{C}, \mathcal{N} : \Omega \to \mathbb{R}^{3\times3\times3\times3}$ are fourth order tensors which generalize the material stress response due to strain. Acknowledging symmetry of $\boldsymbol{\sigma}$ and $\boldsymbol{\varepsilon}$, both $\mathcal{C}$ and $\mathcal{N}$ have 36 potential unique values which can be used to represent material response. Though Eq. (6) provides the most general form, material response using simplifying assumptions of orthotropy or transverse isotropy have been used to accurately represent complex anisotropic material response in tissues. In Qin et al. (2013a), a transversely isotropic model was considered where the elastic material response was transversely isotropic while the viscous response was isotropic. Written in Voigt-form, the distortional components of the Cauchy stress (in local coordinate directions) in their model was given as (Sinkus et al., 2005; Qin et al., 2013a):

$$\begin{bmatrix} \sigma_{r,11} \\ \sigma_{r,22} \\ \sigma_{r,33} \\ \sigma_{r,23} \\ \sigma_{r,13} \\ \sigma_{r,12} \end{bmatrix} = \begin{bmatrix} 2\mu_\perp & 0 & 0 & 0 & 0 & 0 \\ 0 & 2\mu_\perp & 0 & 0 & 0 & 0 \\ 0 & 0 & 2\mu_\parallel & 0 & 0 & 0 \\ 0 & 0 & 0 & \mu_\parallel & 0 & 0 \\ 0 & 0 & 0 & 0 & \mu_\parallel & 0 \\ 0 & 0 & 0 & 0 & 0 & \mu_\perp \end{bmatrix} \begin{bmatrix} \varepsilon_{r,11} \\ \varepsilon_{r,22} \\ \varepsilon_{r,33} \\ 2\varepsilon_{r,23} \\ 2\varepsilon_{r,13} \\ 2\varepsilon_{r,12} \end{bmatrix} + \begin{bmatrix} 2\zeta & 0 & 0 & 0 & 0 & 0 \\ 0 & 2\zeta & 0 & 0 & 0 & 0 \\ 0 & 0 & 2\zeta & 0 & 0 & 0 \\ 0 & 0 & 0 & \zeta & 0 & 0 \\ 0 & 0 & 0 & 0 & \zeta & 0 \\ 0 & 0 & 0 & 0 & 0 & \zeta \end{bmatrix} \frac{\partial}{\partial t} \begin{bmatrix} \varepsilon_{r,11} \\ \varepsilon_{r,22} \\ \varepsilon_{r,33} \\ 2\varepsilon_{r,23} \\ 2\varepsilon_{r,13} \\ 2\varepsilon_{r,12} \end{bmatrix} \tag{7}$$

and the potentially anisotropic mass constitutive equation (*e.g.* replacing Eq. (2)) of

$$\lambda\nabla \cdot \mathbf{u}_r + \xi\frac{\partial}{\partial t}\nabla \cdot \mathbf{u}_r - p_r = 0, \tag{8}$$

---

[3] Here we let $\mathbf{x} \in \Omega$ denote coordinates within the domain, with components $\mathbf{x} = x_1\mathbf{e}_1 + \cdots + x_3\mathbf{e}_3$ and $\nabla = \mathbf{e}_1\frac{\partial}{\partial x_1} + \cdots + \mathbf{e}_3\frac{\partial}{\partial x_3}$ denote the corresponding gradient operator (where $\mathbf{e}_1, \ldots \mathbf{e}_3$ denote the base vectors in $\mathbb{R}^3$).

where λ represents the first Lamé parameter and ξ is the viscosity of the longitudinal wave. In this formulation, the material is considered to be stiffer/softer along fibres aligned with $\mathbf{e}_3$ (with the stiffness parameter $\mu_\parallel$) than in the transverse $\mathbf{e}_1, \mathbf{e}_2-$directions (with stiffness parameter $\mu_\perp$). As an important distinction, within the original model, these constitutive equations were integrated with the momentum balance to give equations describing the motion relative to the local microstructural directions (assumed to align with $\mathbf{e}_3$). The practical application of this form was then to rotate all terms within the equation into the localised coordinate frame, implicitly assuming that the anisotropic orientation of the material is locally constant in space.

A more general approach is to perform rotations within the definition of the distortional Cauchy stress. In this case, it can be easily shown that the model above can be generalised to the form,

$$\begin{aligned}\boldsymbol{\sigma}_r(\boldsymbol{\varepsilon}_r) &= 2\mu_\perp\boldsymbol{\varepsilon}_r^\perp + 2\mu_\parallel\boldsymbol{\varepsilon}_r^\parallel + 2\eta\dot{\boldsymbol{\varepsilon}}_r,\\ \sigma_{r,ij} &= 2\mu_\perp\varepsilon^\perp_{r,ij} + 2\mu_\parallel\varepsilon^\parallel_{r,ij} + 2\eta\dot{\varepsilon}_{r,ij}\end{aligned} \tag{9}$$

where the subscript $\perp$ and $\parallel$ denote the tensor transforms, shown below, which isolate components along and across fibres,

$$\boldsymbol{\varepsilon}_r^\perp = (\mathbf{I} - \mathbf{f}\otimes\mathbf{f})\,\boldsymbol{\varepsilon}_r\,(\mathbf{I} - \mathbf{f}\otimes\mathbf{f}), \tag{10}$$

$$\boldsymbol{\varepsilon}_r^\parallel = \boldsymbol{\varepsilon}_r - \boldsymbol{\varepsilon}_r^\perp. \tag{11}$$

In this form, $\mathbf{f} : \Omega \to \mathbb{R}^3$ denotes the local fibre direction at any point in the material. It is important to note that Eq. (7) expresses the distortional Cauchy stress in local microstructural directions, *i.e.* it assumes that the strain tensor, $\boldsymbol{\varepsilon}_r$, is rotated such that $\boldsymbol{e}_3$ is aligned with fibres and provides the stress aligned with fibres. This form was used in Sinkus et al. (2005); Qin et al. (2013a) by effectively rotating momentum equations and assuming commutativity of rotations. In contrast, Eq. (9) describes the distortional Cauchy stress in physical coordinates, eliminating the need for rotation of the momentum equations or assumptions about the variability of rotations. The resultant complex distortional Cauchy stress is then given by,

$$\boldsymbol{\sigma}(\boldsymbol{\varepsilon}) = G'_\perp\boldsymbol{\varepsilon}^\perp + G'_\parallel\boldsymbol{\varepsilon}^\parallel + iG''\boldsymbol{\varepsilon}, \tag{12}$$

with $\boldsymbol{\varepsilon}^\perp$ and $\boldsymbol{\varepsilon}^\parallel$ defined analogously to their real counterparts as shown in Eqs. 10 and 11.

2.2. Divergence-free FEM reconstruction for anisotropic materials

In this section, we integrate the finite element reconstruction approach detailed in Fovargue et al. (2018a) with the transversely isotropic model introduced in the previous section to enable estimation of stiffness in this class of anisotropic materials. A review of the basic derivation, including the transversely isotropic form in Eq. (12), is outlined (section 2.2.1) along with its practical application to images (section 2.2.2). Finally, we introduce an extension enabling integration of one or more datasets (section 2.2.3).

2.2.1. Derivation of weakform minimisation problem

To estimate the material stiffness, we transform the strong form shown in Eqs. 1-4 into a weakform minimisation problem. Consider a local region $\Omega_L \subset \Omega$ (with boundary Γ_L) around a point for which the material properties are to be estimated. Following the standard weak form derivation, Eq. (1) can be multiplied by a test function, $\mathbf{w}$, and integrated over the local region Ω_L. Applying integration by parts, on the stress and hydrostatic pressure terms, then any solution $(\mathbf{u}, p) \in \mathcal{U} \times L^2_{\mathbb{C}}(\Omega_L)$ satisfies,

$$\int_{\Omega_L} \rho\omega^2\mathbf{u}\cdot\mathbf{w} - \boldsymbol{\sigma}(\boldsymbol{\varepsilon}) : \nabla\mathbf{w} - p\nabla\cdot\mathbf{w}\,d\boldsymbol{x} + \int_{\Gamma_L} \mathbf{t}\cdot\mathbf{w}\,d\boldsymbol{x} = 0 \tag{13}$$

for any $\mathbf{w} \in \mathcal{U}$ (where $\mathcal{U} = \boldsymbol{H}^1_{\mathbb{C}}(\Omega_L)$ is the first Hilbert space for complex vector functions and $L^2_{\mathbb{C}}(\Omega_L)$ is the Banach space for complex scalar functions). Here $\mathbf{t}$ denotes the boundary traction resulting from integration by parts and the complex distortional Cauchy stress is given by Eq. (12). As both the hydrostatic pressure, p, and traction, $\mathbf{t}$, are typically unknown, applying Eq. (13) directly to estimate material characteristics $(G'_\perp, G'_\parallel, G'')$ would require estimation of these quantities as well. Therefore, to solve for the shear parameters only and omit components of the longitudinal wave, test functions, $\mathbf{w}$, were selected from the subset $\mathcal{U}_{0,div} \subset \mathcal{U}$ where

$$\mathcal{U}_{0,div} = \left\{\mathbf{v}\in\mathcal{U} \,\middle|\, \begin{array}{l}\mathbf{v} = \mathbf{0} \text{ on } \Gamma_L;\\ \int_{\Omega_L} q\nabla\cdot\mathbf{v}d\boldsymbol{x} = 0, \quad \forall q \in L^2_{\mathbb{C}}(\Omega_L)\end{array}\right\}, \tag{14}$$

and Eq. (13) simplifies to

$$\int_{\Omega_L} \rho\omega^2\mathbf{u}\cdot\mathbf{w} - \boldsymbol{\sigma}(\boldsymbol{\varepsilon}) : \nabla\mathbf{w}\,d\boldsymbol{x} = 0, \quad \forall\mathbf{w}\in\mathcal{U}_{0,div} \tag{15}$$

where the remaining unknowns are only the material parameters $(G'_\perp, G'_\parallel, G'')$. Assuming local homogeneity of the material properties, and defining

$$\mathcal{L}(\mathbf{w}; G'_\perp, G'_\parallel, G'') = \int_{\Omega_L} \rho\omega^2\mathbf{u}\cdot\mathbf{w} - \boldsymbol{\sigma}(\boldsymbol{\varepsilon}) : \nabla\mathbf{w}\,d\boldsymbol{x} \tag{16}$$

the estimate of material parameters can be written as

$$\begin{aligned}(G'_\perp, G'_\parallel, G'') = \mathbf{arg}\ \min\Big\{\ \mathbf{sup}\Big\{&|\mathcal{L}(\mathbf{w}; G_1, G_2, G_3)|,\\ &\mathbf{w}\in\mathcal{U}_{0,div},\ \|\mathbf{w}\| = 1\Big\},\ G_i \in \mathbb{R}\Big\}.\end{aligned} \tag{17}$$

2.2.2. Image-based application

Typical MRE images provide measurements of the harmonic displacement data across a three-dimensional grid of voxels. Hence, the measured complex harmonic displacement, $\hat{\mathbf{u}}$, can be related to the true displacements satisfying Eqs. 1-4, by relating the voxel indexed entries $\boldsymbol{i} = (i, j, k)$ and pixel dimensions (h_1, h_2, h_3) to physical positions in space (x_1, x_2, x_3). Noting that some discrepancy and/or error, $\boldsymbol{\epsilon}$, exists between the data and displacement due to discretisation, noise, voxel averaging, and other imaging artefacts, the two can be related by

$$\hat{\mathbf{u}}(\boldsymbol{i}) = \mathbf{u}(h_1 i, h_2 j, h_3 k) + \boldsymbol{\epsilon}(\boldsymbol{i}). \tag{18}$$

In addition, while $\mathbf{u}$ denotes continuous data on which differential operators can be applied, $\hat{\mathbf{u}}$ is only defined discretely at pixels. Limiting the influence of noise in the MR images is often accomplished by applying a low pass filter such as Gaussian smoothing, which here is included as an optional pre-processing step. Smoothing is applied in a standard three dimensional way by reassigning voxel values based on some chosen convolution kernel and applied directly to the displacement data, $\hat{\mathbf{u}}$.

Following the approach and notation in Fovargue et al. (2018a), derivatives of $\hat{\mathbf{u}}$ are approximated using the approach in Honarvar et al. (2016) where data is locally approximated through polynomial fitting and the differential operator is applied to the fit. Letting $\nabla\hat{\mathbf{u}} = D_{pf}(\hat{\mathbf{u}}; \nabla)$ denote the gradient approximated using this polynomial fitting approach, the small strain tensor can be approximated as

$$\hat{\boldsymbol{\varepsilon}}(\boldsymbol{i}) = \frac{1}{2}[\nabla\hat{\mathbf{u}}(\boldsymbol{i}) + \nabla\hat{\mathbf{u}}^T(\boldsymbol{i})]. \tag{19}$$

Using knowledge of the local fibre orientations, $\hat{\mathbf{f}}(\boldsymbol{i})$ coming from image data, a similar transform can be applied to $\hat{\boldsymbol{\varepsilon}}(\boldsymbol{i})$ to compute its perpendicular and parallel counterparts, *e.g.*

$$\hat{\boldsymbol{\varepsilon}}^\perp(\boldsymbol{i}) = (\mathbf{I} - \hat{\boldsymbol{f}}(\boldsymbol{i})\otimes\hat{\boldsymbol{f}}(\boldsymbol{i}))\,\hat{\boldsymbol{\varepsilon}}(\boldsymbol{i})\,(\mathbf{I} - \hat{\boldsymbol{f}}(\boldsymbol{i})\otimes\hat{\boldsymbol{f}}(\boldsymbol{i})), \tag{20}$$

$$\hat{\boldsymbol{\varepsilon}}^{\parallel}(\boldsymbol{i}) = \hat{\boldsymbol{\varepsilon}}(\boldsymbol{i}) - \hat{\boldsymbol{\varepsilon}}^{\perp}(\boldsymbol{i}). \tag{21}$$

To estimate stiffness at each image pixel, the minimisation problem in Eq. (17) must first be adapted to the discrete image data. This is done using a finite element discretisation over a compact kernel, Ω_L^h, comprised of tetrahedral elements using the inf-sup stable $\mathbb{P}^2 - \mathbb{P}^1$ basis functions for displacement and pressure, respectively (see Fovargue et al. (2018a)). Fields for displacement and strain are interpolated on Ω_L^h using $\mathbb{P}^2$, with nodal values extracted from the underlying image voxel data. Letting U, $\nabla\mathcal{E}^*$, and P denote the complex displacements, small strains (or its projected variants), and pressures at nodes, the continuous weakform in Eq. (13) can be written as a linear system,

$$\begin{aligned} &\rho\omega^2 W^T\mathbf{M}U - G'_{\perp}W^T\mathbf{K}\mathcal{E}^{\perp} - G'_{\parallel}W^T\mathbf{K}\mathcal{E}^{\parallel} \\ &-iG''W^T\mathbf{K}\mathcal{E} - W^T\mathbf{B}^T P = 0, \end{aligned} \tag{22}$$

where W denotes the nodal values of any test function we select (assuming values are zero on the external boundary of Ω_L^h). Here, $\mathbf{M}$ and $\mathbf{B}^T$ denote the classical discrete mass matrix and divergence matrices. While in standard FEM, $\mathbf{K}$, would denote the stiffness matrix, here the small strain is interpolated directly from the image (with standard derivatives computed for the test field). From this form, the subset of divergence free test functions can be constructed by examining the nullspace of $\mathbf{B}$, denoted by $\mathbf{X}$. Hence, restricting W to only functions that are in the nullspace of $\mathbf{B}$, reduces to multiplication through the system by $\mathbf{X}$.

The continuous minimisation problem in Eq. (17), can then be recast on the image (pixel-by-pixel), by least-squares minimisation of the vector functional

$$\boldsymbol{\mathcal{L}}_h(G'_{\perp}, G'_{\parallel}, G'') = \rho\omega^2\mathbf{XM}U - \mathbf{XK}(G'_{\parallel}\mathcal{E}^{\parallel} + G'_{\perp}\mathcal{E}^{\perp} + iG''\mathcal{E}) \tag{23}$$

making the estimate of material parameters

$$(G'_{\perp}, G'_{\parallel}, G'') = \mathbf{arg}\ \min\left\{ \|\mathcal{L}_h(\mathbf{w}; G_1, G_2, G_3)\|,\ G_i \in \mathbb{R} \right\}. \tag{24}$$

2.2.3. Multi-Image Inclusion

In the case where multiple wave images are collected on the same body, the transversely isotropic divergence-free FEM reconstruction can be easily augmented by extending the vector functional, $\boldsymbol{\mathcal{L}}_h$. Suppose that M images are collected, for which the i^{th} image yields the displacement vector U_i and strain vector $\mathcal{E}_i$ (as well as $\mathcal{E}_i^{\perp}$ and $\mathcal{E}_i^{\parallel}$), then

$$\boldsymbol{\mathcal{L}}_h^{\star}(G'_{\perp}, G'_{\parallel}, G'') = \rho\omega^2\mathbf{XMU} - \mathbf{XK}(G'_{\parallel}\boldsymbol{\mathcal{E}}^{\parallel} + G'_{\perp}\boldsymbol{\mathcal{E}}^{\perp} + iG''\boldsymbol{\mathcal{E}}) \tag{25}$$

where (for $k = \parallel, \perp, {\prime\prime}$),

$$\boldsymbol{U} = \begin{bmatrix} U_1 \\ \vdots \\ U_M \end{bmatrix}, \quad \boldsymbol{\mathcal{E}}^k = \begin{bmatrix} \mathcal{E}_1^k \\ \vdots \\ \mathcal{E}_M^k \end{bmatrix}, \tag{26}$$

and the three unique stiffness parameters are estimated by the least-squares minimisation of $\boldsymbol{\mathcal{L}}_h^{\star}$ as shown in Eq. (24).

2.3. In silico testing

As real tissue data can involve complex distributions of anisotropy, heterogeneous stiffness and data artefacts such as noise, a simple *in silico* phantom was established within which these complications could be incrementally analyzed, providing a clear platform for understanding the reconstruction's strengths and limitations. In the simplest case, experiments were run with a uniform fibre orientation, a single loading condition and no added noise. The *in silico* model was varied to represent more complex fibre distributions, multiple sources of wave loading, noise in both the wave and fibre data and varying viscosity. Each factor was altered to encompass variations that represent *in vivo* conditions. The *in silico* experiment allows us to vary each parameter independently in order to understand which has the greatest impact on accuracy and variability of the stiffness parameter estimates.

2.3.1. In silico phantom

For the *in silico* experiments, an anisotropic cube (40x40x40 mm) was embedded in a larger cube (100x100x100 mm), which is composed of a purely isotropic material (Fig. 1a, top). Boundary conditions were specified, either a normal or shear displacement, over a patch on one of three faces to model the placement of a vibrating transducer (Fig. 1a, bottom). These different boundary conditions will be referred to as wave motions (WM). As presented in the previous section, the elastic component was considered to be transversely isotropic within the central cube, whereas the viscous component is isotropic and constant throughout the entire domain. In the anisotropic region, two elastic parameters are reconstructed, $G'_{\parallel}$ and $G'_{\perp}$, along with one viscous parameter, G''. In the isotropic region, one elastic parameter is reconstructed, G', along with a viscous parameter.

The directionality within the transversely isotropic region is defined by one of six fibre fields, which progress from a simple (FD1) to more complex distribution (FD6) (Fig. 1b). For further details regarding the fibre distributions, see the *Supplementary Materials*. All *in silico* experiments were simulated in **CHeart** (Lee et al., 2016).

2.3.2. In silico analysis

In the anisotropic region, $G'_{\parallel}$ and $G'_{\perp}$ were set to 4 kPa and 2 kPa, respectively to reflect a material which is stiffer along the fibre direction. The isotropic region was given a stiffness of 3 kPa. Stiffness parameters were also varied spatially to examine spatial heterogeneity in transversely isotropic stiffness parameters (see *Supplementary Materials*). Experiments were replicated for uniform viscosity values of G'' of 0.5 kPa, 1 kPa and 1.5 kPa. As G'' naturally varies in tissues, these values were selected to reflect a range common in biological tissue (Chakouch et al., 2016; Klatt et al., 2010). Stiffness maps with true parameters are shown in Figure S2.

Fifty image slices were generated from the resulting displacement fields from *in silico* simulations with an isotropic resolution of 2x2x2 mm. However, only nine slices, taken from the central region of the block, were used to test the reconstruction. These nine slices encompassed the anisotropic inclusion as well as the surrounding isotropic regions within those image planes. In all tests, stiffness maps are shown for $G'_{\parallel}$, $G'_{\perp}$ and G'' in a single image slice which cuts through the anisotropic region (shown in orange in Fig. 1a). Additionally, error plots illustrate the mean and one standard deviation of each estimated parameter shown alongside the true value for comparison.

Multiple tests were run using this *in silico* experiment in order to understand the effects of important factors, such as fibre orientation and variation, viscosity and modes of wave transduction, on reconstruction accuracy. Reflecting the potential limitations in data, a set of sensitivity analyses were also performed by considering different degrees of noise on the *in silico* wave data as well as the fibre distributions. A comprehensive breakdown of these tests is presented in the *Supplementary Materials*, with key results shown in the main manuscript.

2.4. Ex vivo testing

Ex vivo experiments were also used to assess the accuracy of the proposed reconstruction method. MR elastography, DTI and mDixon images were acquired from a sample of bovine muscle using a 3T Philips Ingenia CX (Philips Healthcare, Best, The Netherlands) and were used to estimate tissue stiffness. A Kinexus rotational rheometer (Malvern Instruments, UK) was also used to cal-

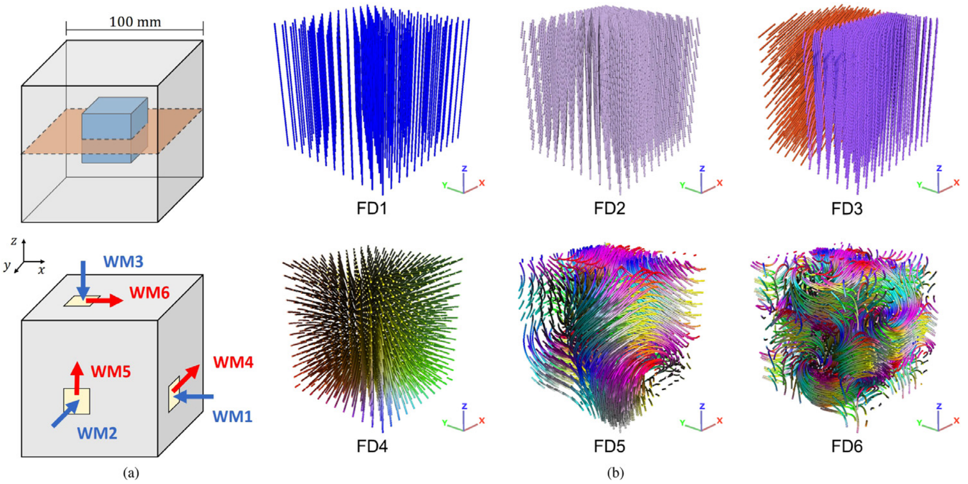

Fig. 1. (a) Schematics of the computational domain and loading conditions of the *in silico* phantom. (top) The smaller cube of transversely isotropic material is centered within a larger cube made of an isotropic material. The orange slice represents the *in silico* imaging plane shown in the results throughout the paper and supplement. (bottom) The location and types of boundary conditions are shown. Wave motions 1-3 (blue) are applied compression, whereas 4-6 (red) correspond to applied shear displacements. (b) Images of all six fibre distributions. The plots are restricted to the region of the domain containing fibres. For planar X-Y views of each fibre field taken at the orange slice, see Figure S1.

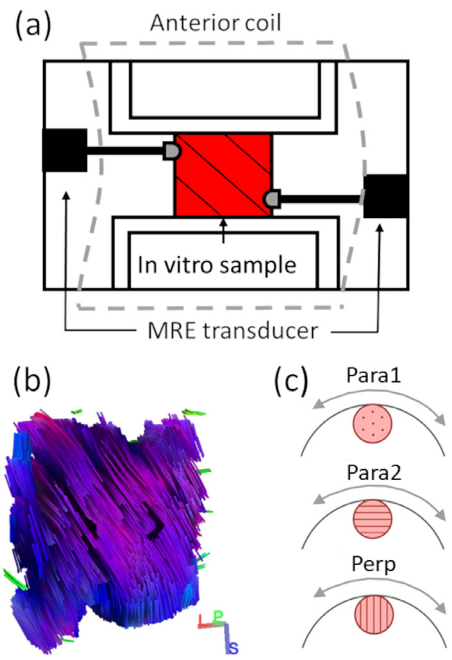

Fig. 2. Ex vivo muscle experiments (a) Schematic of MRE set-up for *ex vivo* testing. MRE transducer coils are mounted outside the imaging field of view. The two probes apply vibrations to the phantom at contralateral positions (in separate acquisitions). (b) Fibre tracts for the bovine muscle sample. (c) Schematic showing the fibre directions of the *ex vivo* samples during the eccentric rheometry, the grey arrows indicate the direction of the applied shear, where both samples Para 1 and Para 2 are sheared along the direction of the fibres, whereas Perp samples are loaded transversely to the fibres.

culate to the material properties of samples taken from the same bovine muscle.

2.4.1. Ex vivo muscle tissue

A bovine muscle tissue sample (*biceps femoris*) was cut into 10x10x9 cm cuboids. The sample was regularly sprayed with a 0.9% phosphate buffered saline solution to prevent swelling or shrinkage (Nicolle and Palierne, 2010). The sample was placed into the centre of the test rig (Fig. 2). The side walls of the testing apparatus were positioned in contact with the sample to restrict off-axis and rigid body motion (shown in Fig. 2 on top and bottom). MRE coils were mounted on either side of the sample, with the probes in contact with both sides of the sample, offset to be contralateral (Fig. 2a). During imaging, the dStream 32 channel torso coil was placed over the test rig and used in combination with the posterior coil. Table 1 details the scanning parameters for each sequence.

2.4.2. Magnetic resonance elastography data acquisition

The driving coils of the MRE transducer were connected to a function generator (33210A Agilent, California, USA) synchronised to the scanner. Applying a sinusoidally varying current to the coils, the transducer oscillated and induced vibrations via the guided rod in contact with the tissue (Fig. 2a). Only one transducer was triggered while scanning. The scan was then repeated only triggering the other transducer.

MR elastography scans acquired three phase images encoding displacements in one of three orthogonal directions as well as one reference phase image with no direction encoding. A driving frequency of 70 Hz was used, sampling the sinusoidal wave at eight time dynamics. The images were collected in the transverse plane, positioned in the centre of the sample. The raw displacement data was first unwrapped and smoothed with a Gaussian smoothing filter using a 3x3x3 voxel convolution kernel before reconstruction.

2.4.3. Anatomical imaging

To help visualise fat and connective tissue within the sample and for defining regions of interest (ROI), a two-point mDIXON fast field echo (FFE) scan was acquired. Twenty-seven slices, covering the whole leg volume, were acquired in a transverse plane, with the image stack centre matching the MRE scans.

2.4.4. Diffusion tensor imaging and tractography

Diffusion data were acquired with a single shot EPI sequence with 32 diffusion direction, taken with the same field of view (FOV), voxel size and location as the MRE images. The b factor was 500 s/mm^2. All other scanning parameters are detailed in Table 1. The DTI images were filtered using a local principal component analysis (LPCA) filter (Manjón et al., 2013) and susceptibility and eddy-current induced distortions were corrected using FMRIB Software Library's (FSL) eddy tool (Andersson et al., 2003). To correct for small distortions that remain, Elastix registration software

Table 1
MR imaging parameters used in mDixon, MRE and DTI sequences for the *ex vivo* and *in vivo* imaging acquisitions.

	Ex vivo			*In vivo*		
	mDIXON	MRE	DTI	mDIXON	MRE	DTI
TR/TE(/TE2) [ms]	6/2.37/1.19	130.4/9.21	3600/80	4.15/2.37/1.19	182.5/9.21	3600/80
Field of view (FOV) [mm]	160x160	160x160	160x160	192x192	192x192	192x192
Matrix	224x224	80x80	80x80	192x192	64x64	64x64
Flip angle [°]	6	30	90	5	30	90
Number of slices	30	9	9	41	9	9
In-plane resolution [mm^2]	0.71x0.71	2x2	2x2	1x1	3x3	3x3
Slice thickness [mm]	2	2	2	3	3	3

(v4.8, Klein et al. (2010)) was used to apply an affine transformation to the DTI images to align them with the MRE data.

In order to provide consistent and robust fibre orientations across the muscle for the anisotropic reconstruction, tractography was used to identify muscle fibre directions. Muscle fibre tracts (Fig. 2b) were estimated using a deterministic tractography algorithm provided in DSI studio (Yeh et al., 2013). Tracts were randomly seeded, resulting in 9000 tracts per data set. Additional tractography parameters include turning angle = 10°, length = 10 to 300 mm, and the FA threshold = 0.0008. To assign a fibre direction to each voxel in the reconstruction, the fibre tracts were down-sampled and the average direction for a voxel was calculated. A discrete cosine transform-based penalised least squares approach was then used to smooth the vector field (Garcia, 2010; 2011).

2.4.5. Rheometry

To validate the MRE reconstruction, a sample of bovine muscle tissue was tested using rheometry and MRE. Prior to imaging, a section of the same muscle was dissected into nine cylindrical samples (10 mm diameter and 2 mm thick), from regions of the muscle that appeared homogeneous. The samples were then placed eccentrically at the edge of the 40 mm diameter plate of a Kinexus rotational rheometer (Malvern instruments, UK), either with the fibres parallel or perpendicular to the direction of the applied shear strain (Fig. 2c). The samples were preloaded with 10% compressive strain, to reduce slip. Samples were preconditioned for ten cycles at 0.1 Hz and 0.01% strain, to establish a uniform initial tissue state. A frequency sweep was then performed at 0.01% strain from 0.1 to 10 Hz. To account for the eccentric loading of the sample a correction factor was applied to the calculated moduli (Tan et al., 2015; Cirka et al., 2012). Further details of the experimental set-up and data processing have been previously described in Tan et al. (2015).

2.5. *In vivo* testing

Change in ankle position (angle between the foot and shank) has been shown to passively stretch muscles in the lower leg, increasing fascicle length and changing the pennation angle (Bolsterlee et al., 2017). To demonstrate that the proposed anisotropic reconstruction method can be used to detect changes in muscle stiffness, six healthy subjects with no contraindications for MRI were enrolled in the study (2 M : 4 F; age 49±13 years; weight 88±17 kg; height 170±9 cm; mean ± S.D), and underwent imaging of the right lower leg with their ankle in both a relaxed and two maximally flexed positions to put lower leg muscles under tension.

All experimental protocols were approved by the University of New South Wales' Human Research Ethics Committee (approval HC15821), and they were conducted according to the Declaration of Helsinki (2015) with the exception of clause 35. All participants gave written and informed consent. Imaging for the *in vivo* experiments was performed with a 3T Philips Achieva TX (Philips Healthcare, Best, The Netherlands) (see Table 1 for scanning parameters for each sequence). Participants were positioned supine and feet first on the MR scanner bench. The foot was strapped to an MRI-compatible footplate in a neutral position (90° between the foot and shank) where the muscles were assumed to be slack (Fig. 3a). The MRE coils were mounted on top of the MR compatible footplate, and the probe was placed flat against the distal end of the tibia. During imaging, the SENSE Flex-L coils were placed about the calf on the outside of the right and left walls of the footplate. Scanning was repeated with the foot plate repositioned so that the foot was maximally plantarflexed (increased ankle angle; Fig. 4a) or dorsiflexed (decreased ankle angle; Fig. 4a), putting either the tibialis anterior (TA) or the soleus (SOL) and medial gastrocnemius (MG) under tension, respectively (Fig. 4b).

2.5.1. Magnetic resonance elastography data acquisition

For the *in vivo* scans, a driving frequency of 50 Hz was used, sampling the sinusoidal wave at eight time dynamics. The scan was positioned in an oblique sagittal plane, covering a 27 mm thick section between the tibia and fibula (Fig. 3b). The FOV spanned from the lateral condyle of the tibia to the lateral malleolus. Similarly to the *ex vivo* experiments, the raw data was first unwrapped and smoothed prior to reconstruction.

2.5.2. Anatomical imaging

mDIXON images were acquired in an oblique plane, centred between the tibia and fibula (Fig. 3b) similar to MRE scans, and 41 slices were collected to cover the whole volume of the lower leg. These images were used for defining the ROIs as well as reference images to improve the registration between the MRE and diffusion images.

2.5.3. Diffusion tensor imaging and tractography

For the *in vivo* experiments, 32 diffusion-weighted images were also acquired with the same FOV, voxel size, and in the same location as the MRE scans. The b factor was 500 s/mm^2. All other scanning parameters are detailed in Table 1. An LPCA filter was used to denoise the raw diffusion images. To correct minor offsets and image distortions, an affine transformation was applied to the diffusion data. The diffusion data was first registered to the water-phase mDIXON image. Due to the similarity in contrast, the out-of-phase images were then used to register the mDixon scans to the MRE. Finally, the same affine transform was applied to the DTI data, to ensure it was aligned with the MRE images.

The same tractography parameters previously described were also used for the *in vivo* data set, but with an FA threshold of 0.08. The resulting tracts were then down-sampled and smoothed to provide the fibre directions for the reconstruction. Fig. 4b demonstrates the fibre distribution when the calf muscles were in different states of flexion for a representative subject.

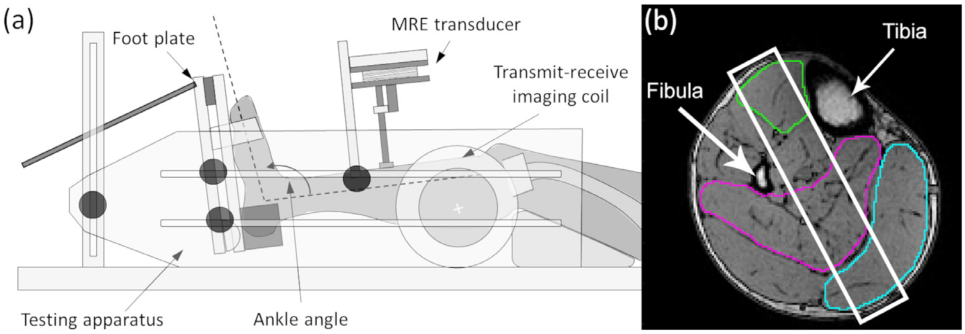

Fig. 3. In vivo experiments (a) Schematic of MRE transducer set-up for *in vivo* testing. MRE coils are connected to the walls of the MR compatible foot plate. The position of the coils can be adjusted so that the MRE probe is flat against the distal end of the tibia. The foot plate is fixed in position during scans. Between scans, the foot plate can be moved to stabilise the foot in either a plantarflexed or dorsiflexed position. The black circles in the image indicate hand screws, which fix the foot plate and the mounting frame of the transducer in position. (b) Axial scan used to find the oblique plane between the tibia and fibula, for the MRE and DTI scans (white); the 3D anatomical mDixon images are also centred on this plane. The tibialis anterior (TA), soleus (SOL) and medial gastrocnemius (MG) are highlighted in green, pink and blue, respectively.

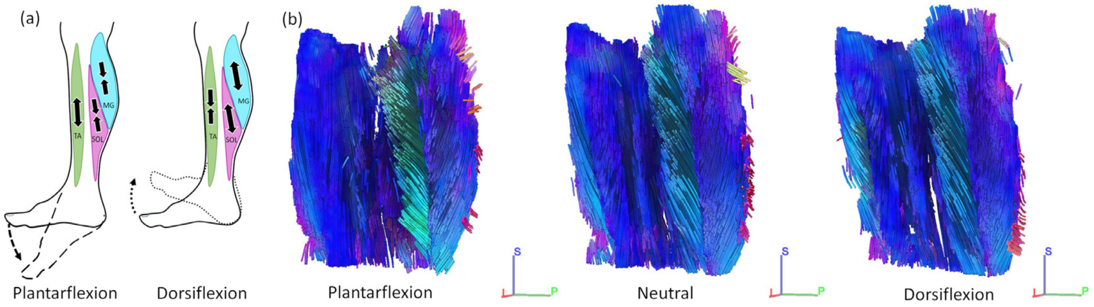

Fig. 4. (a) A schematic demonstrating how ankle position stretches muscles. When the foot is plantarflexed (pulled away from the body), the TA is put under tension, whereas the SOL and MG are unloaded. With the foot in dorsiflexion, the TA is unloaded, but the SOL and MG are in tension. (b) Images of the muscle fibre directions when the ankle is in a plantarflexed, neutral and dorsiflexed position. Note that the muscles are mostly oriented in the superior-inferior (blue), and anterior-posterior (green) directions. When in tension, the fibres elongate in the superior-inferior direction.

2.5.4. In vivo analysis

ROIs of the TA, SOL and MG were segmented from the mDIXON water images using SASHIMI segmentation v1.1 (Developed in Matlab R2019b, and freely available on GitHub: github.com/bartbols/SASHIMI). The ROIs were used to calculate the mean and standard deviation of the shear moduli for each muscle in the three positions. The cohort mean ± SD intervals are used to compare the effect of ankle position on muscle stiffness. The quality of the MRE displacement data was assessed in terms of its 'nonlinearity'. Nonlinearity provides an indication of the proportion of vibration-related energy at each voxel that is not at the driving frequency, where a greater value indicates a higher contribution of different frequency components and overall noisier data. Any voxel with a nonlinearity greater than 35% was excluded from the ROI. Any muscle with more than 50% of the voxels removed was excluded from group analysis. A one-way ANOVA with a Bonferroni post-hoc test was used to assess the effect of ankle position on shear moduli of each muscle, considering $P < 0.05$ to be statistically significant (IBM SPSS Statistics v24, IBM Corp., Armonk, NY, USA).

3. Results

3.1. In silico results

3.1.1. Influence of multi-image reconstruction

In this test (Fig. 5), the second fibre distribution (FD2) was used to illustrate the benefit of using wave data from multiple simulations with different loading conditions. The reconstruction was performed using results from (a) a single simulation with the x-direction compression (WM1), (b) two simulations with compression in the x- and y-directions (WM1 + WM2), respectively and finally (c) three simulations with compression applied in the x-, y-, and z-directions (WM1 + WM2 + WM3), respectively. In general, the ability to reconstruct accurate anisotropic stiffness with a single wave mode is dependent on the fact that the waves, in the *in*

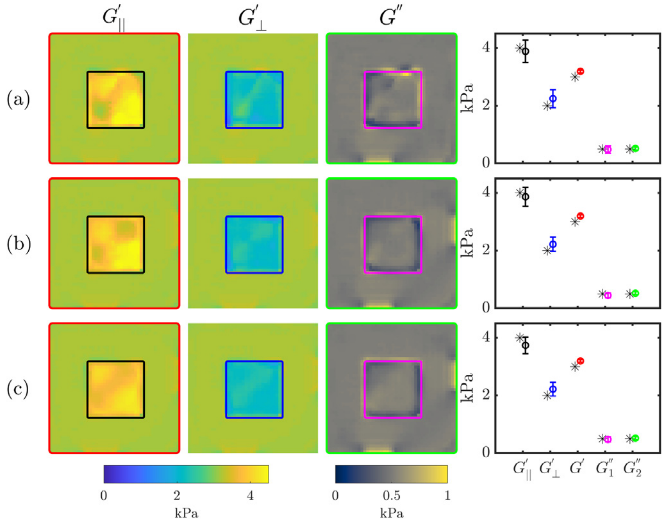

Fig. 5. Reconstructed shear moduli maps and comparisons to ground truth for FD2 with single and multiple wave modes used for reconstruction: (a) WM1 (b) WM1 + WM2 (c) WM1 + WM2 + WM3. From left to right are images of $G'_{\|}$, $G'_{\perp}$ and G'' stiffness reconstructions followed by comparisons with ground truth values. G''_1 and G''_2 are the viscous parameters inside and outside of the anisotropic inclusion respectively. Coloured symbols correspond to the mean / standard deviation values averaged across the corresponding coloured boxes in the stiffness maps. Results are shown for noise-free wave data and $G'' = 0.5$.

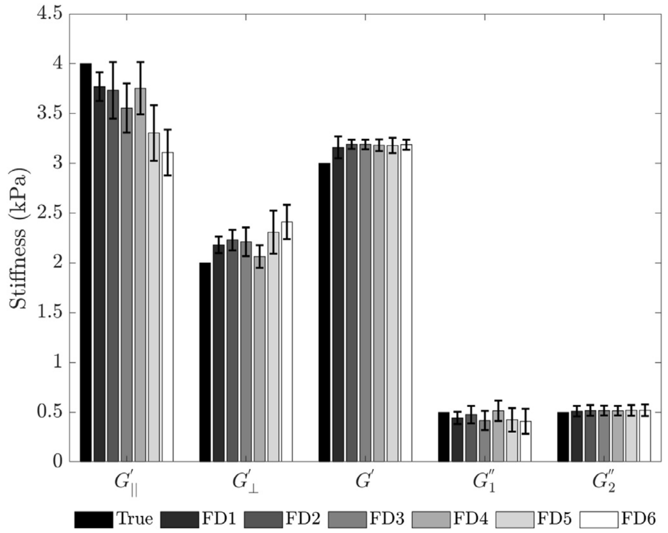

Fig. 6. Comparison of the shear moduli against ground truth ('True', black bar) for each fibre distribution (FD1 - FD6) using WM1+WM2+WM3. Bars represent the mean ± one standard deviation. Results are shown for noise-free wave data and $G'' = 0.5$.

silico setup, occur in a bounded domain, causing reflections which result in a complex wave field that interrogates the material from multiple orientations. Incorporating more wave datasets, however, further reduces the variability in the estimated parameters, which can be seen in the mean plots in Fig. 5. A more comprehensive set of simulation results, including percent RMS error and standard deviation for an increasing number of wave modes for all fibre distributions is found in the supplementary data Section S3.

3.1.2. *Influence of fibre orientation*

Reconstructions of simulated data from the six fibre fields (FD1 - FD6) for various wave modes were performed. Results from reconstructions that utilize three wave modes (*e.g.* WM1 + WM2 + WM3) are illustrated in Fig. 6. It can be seen that there is a limit to the variability of the fibre field that can be reliably reconstructed. For FD1, FD2 and FD4, fibre distributions are either constant or slowly varying, enabling accurate estimation. For more rapidly varying and non-uniform in fibre direction fields (FD5, FD6), the accuracy of the stiffness estimates deteriorates. Quantitatively, the mean estimated $G'_{\parallel}$ stiffness shows an underestimation and $G'_{\perp}$ shows modest overestimation. This is likely due to a combination of limited data resolution as well as the inherent wavelength of the vibrations probing the material. When there are sharp changes in the fibre orientation, as in FD3, the stiffness estimates are accurate, but deterioration near the discontinuity is observed (Figure S10). This is commonly observed in direct reconstruction techniques, particularly those with local stiffness homogeneity assumptions as considered here. Stiffness maps for all fibre distributions can be found in S3.

3.1.3. *Influence of viscosity*

Results from simulations with different viscosities (i.e. loss moduli, $G'' = 0.5$ kPa, 1.0 kPa and 1.5 kPa) indicate that the new reconstruction algorithm accurately estimates the viscous parameters, although as viscosity increases, the variability of shear modulus estimates increases by $1.5 - 2$ fold. However, as %RMSE remains low, errors remain below 10%, 20% and 25% for $G'_{\parallel}$, $G'_{\perp}$ and G'', respectively. Interestingly, use of shear wave modes (*e.g.* WM4-6) generally exhibit a more modest increase with G'', usually between $1.1 - 1.5$ fold. Both observations are potentially due to the enhanced attenuation with higher material viscosity and poorer mode conversion in compression wave modes (WM1-3). Complete results are shown in for FD2 and FD4, with a representative plot shown in Fig. 7 (FD2, with WM1 + WM2 + WM3). Percent RMS error as well as estimated parameter standard deviations with varying viscosity are shown in Figure S15.

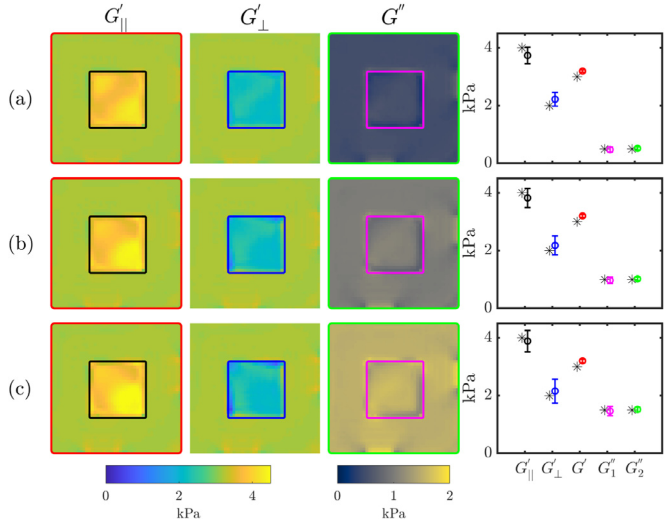

Fig. 7. Reconstructed shear moduli maps and comparisons to ground truth for FD2 with WM1 + WM2 + WM3 for three viscosity values: (a) $G'' = 500$ Pa (b) $G'' = 1000$ Pa (c) $G'' = 1500$ Pa. From left to right are images of $G'_{\parallel}$, $G'_{\perp}$ and G'' stiffness reconstructions followed by comparisons with ground-truth values. G''_1 and G''_2 are the viscous parameters inside and outside of the anisotropic inclusion respectively. Coloured symbols correspond to the mean / standard deviation values averaged across the corresponding coloured boxes in the stiffness maps. Results are shown for noise-free wave data.

3.1.4. *Influence of wave transduction*

It has been shown in previous sections that by combining wave data, improvements in stiffness estimates can be obtained. However, since acquisition of multiple images increases imaging time and presents practical challenges of multi-site wave transduction, it is desirable to understand which wave loading combinations result in the most accurate stiffness estimates. The table below (Fig. 8) shows mean estimated shear stiffness values for $G'_{\parallel}$ and $G'_{\perp}$ for all combinations of wave motion pairs.

The best loading combination pairs for reconstructing $G'_{\parallel}$ and $G'_{\perp}$ were combinations of pushing motions (WM1 and WM2) applied on perpendicular surfaces. However, it is apparent in the figure that (a) there are multiple wave mode combinations which result in low RMS error and (b) the best wave mode combinations for estimating $G'_{\parallel}$ are not necessarily the best combinations for estimating $G'_{\perp}$. In general, the optimal loading combinations are dependent on the fibre distribution, viscosity and amount of noise in the wave field. Further tables and discussion can be found in S5.

3.1.5. *Sensitivity to wave noise*

To test the impact of noise in the displacement images, uniform random noise was added to all components of the wave data. The magnitude of the added noise was given as a percentage, α, of the mean magnitude of the waves inside the inner anisotropic cube of the domain. The tested values were $\alpha = [0.05, 0.1, 0.2]$. After the noise was added, a 3x3x3 Gaussian smoothing filter with a standard deviation of 0.5 was applied. As seen in Fig. 9, with increasing noise, $G'_{\parallel}$ was underestimated whereas estimates of $G'_{\perp}$ (as well as viscosity estimates) were minimally impacted.

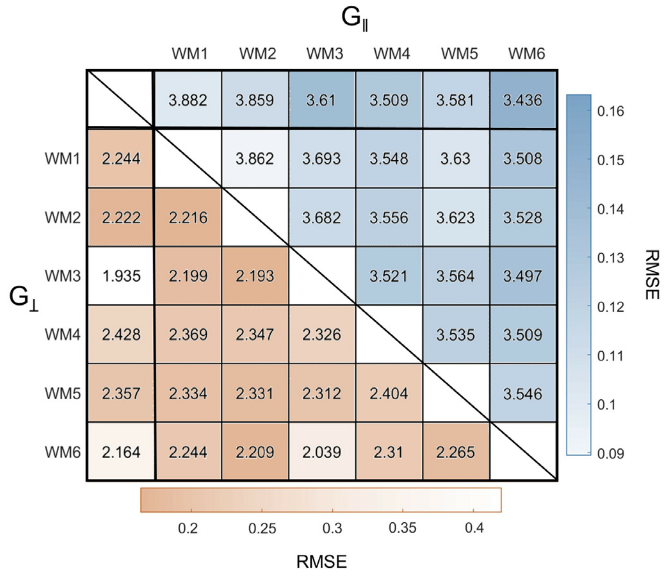

		WM1	WM2	WM3	WM4	WM5	WM6
		3.882	3.859	3.61	3.509	3.581	3.436
WM1	2.244		3.862	3.693	3.548	3.63	3.508
WM2	2.222	2.216		3.682	3.556	3.623	3.528
WM3	1.935	2.199	2.193		3.521	3.564	3.497
WM4	2.428	2.369	2.347	2.326		3.535	3.509
WM5	2.357	2.334	2.331	2.312	2.404		3.546
WM6	2.164	2.244	2.209	2.039	2.31	2.265	

Fig. 8. Comparison of the mean anisotropic shear moduli for loading combination pairs for FD2. Ground truth value for $G'_{\parallel}$ is 4kPa and for $G'_{\perp}$ is 2 kPa. The pairs of wave motions used correspond to the row and column headings. The cells in the top row and the first column represent mean estimated stiffness values using only a single wave motion for comparison. The colour of the cell represents the RMS error over the entire anisotropic region (see scale bars for RMSE in $G'_{\parallel}$ (blue) and $G'_{\perp}$ (orange). Results are shown for noise-free wave data and $G'' = 0.5$.

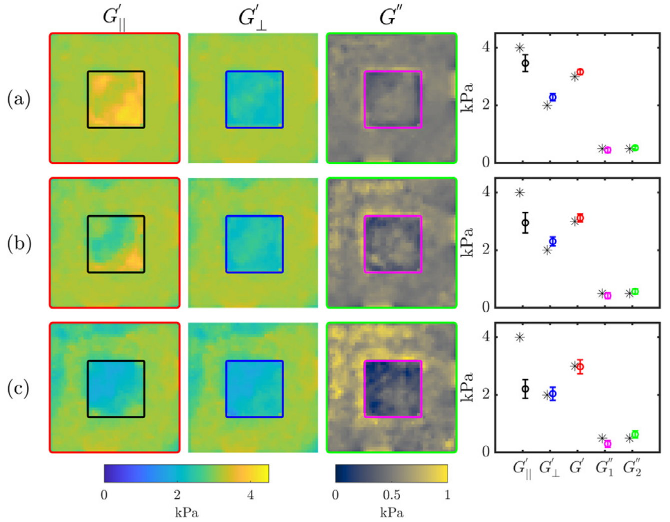

Fig. 9. FD2 with WM1 + WM2 + WM3 applying uniform random noise to the wave displacements: (a) 0.05 (b) 0.1 (c) 0.2. Coloured error bars correspond to values enclosed in the corresponding coloured box in the stiffness maps. Results are shown for $G'' = 0.5$.

3.1.6. Sensitivity to fibre angle noise

Next, uniform random noise ($\alpha = [0.05, 0.1, 0.2]$) was added to each component of the normalised fibre vectors. In contrast to when noise was added to the displacement field, noise in the fibre orientation affected estimates of both $G'_{\parallel}$ and $G'_{\perp}$ (see Fig. 10). With increasing noise, estimates of $G'_{\parallel}$ decreased whereas estimates of $G'_{\perp}$ increased, both converging towards their mean value, likely reflecting that stiffness in an intermediate direction is likely to include contributions from both parallel and perpendicular directions. This test is illustrative of the importance of accurately measuring fibre orientations when reconstructing anisotropic material parameters from MRE.

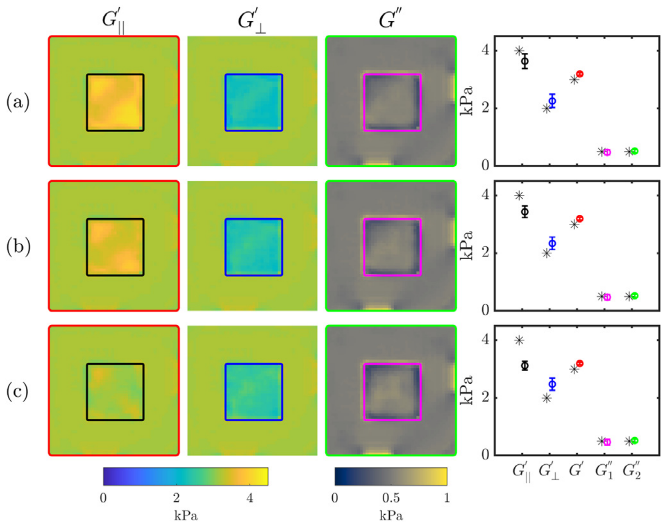

Fig. 10. FD2 with WM1 + WM2 + WM3 applying uniform random noise to the fibre orientation: (a) 0.05 (b) 0.1 (c) 0.2. Coloured error bars correspond to values enclosed in the corresponding coloured box in the stiffness maps. Results are shown for $G'' = 0.5$.

3.1.7. Comparison with previous method

Both the current and a previously presented curl-based approach (Sinkus et al., 2005; Qin et al., 2013b) were used to estimate stiffness parameters for FD4 with different wave motion combinations and amounts of noise. Fig. 11 illustrates that the estimation of $G'_{\parallel}$ by the previous method was more affected by the addition of wave motion noise than the current method. In both methods, the use of multiple waves (WM1-3 versus WM1 only) reduced the variation in estimated parameters. Further results comparing the two methods are presented in S9.

3.2. Ex vivo results

Stiffness estimates for the *ex vivo* tissue, performed both with single and multiple wave mode reconstruction, are shown in Fig. 12. Local differences in stiffness estimates can be seen between WM1 and WM2 in both $G'_{\parallel}$ and $G'_{\perp}$. Similar regional differences are also observed in the *in silico* tests with different loading conditions shown in section S1 of the supplementary material. In the *ex vivo* experiment, including more than one dataset resulted in a small reduction in variation in estimated parameters (Fig. 12). Variability in the estimated parameters also reflects heterogeneity in the muscle sample, including regions of low stiffness that correspond to voids in the *ex vivo* sample (see the mDIXON image in Fig. 12).

Both eccentric rheology and the new anisotropic MRE reconstruction method were used to estimate stiffness parameters of *ex vivo* muscle samples. Due to the large difference between shear rates (i.e. frequency) in the rheometry (max 10Hz) and MRE (70Hz) experiments, and the highly shear rate dependent mechanical behaviour of muscles, direct quantitative comparisons of rheometry and MRE shear moduli measurements are challenging. However, anisotropy is expected to be more stable across frequencies, and thus we have compared the ratio of the parallel and perpendicular shear moduli, as has been done previously (Qin et al., 2013a). These data are shown in Fig. 13, and indicate that the anisotropic ratio is consistent between rheometry and anisotropic MRE measurements of the same bovine muscle tissue. The rheometer measurements also showed that samples loaded both parallel and perpendicular to the muscle fibres had comparable values of G'' (0.9±0.2kPa for both), which supports the assumption of an isotropic viscous response in the reconstruction.

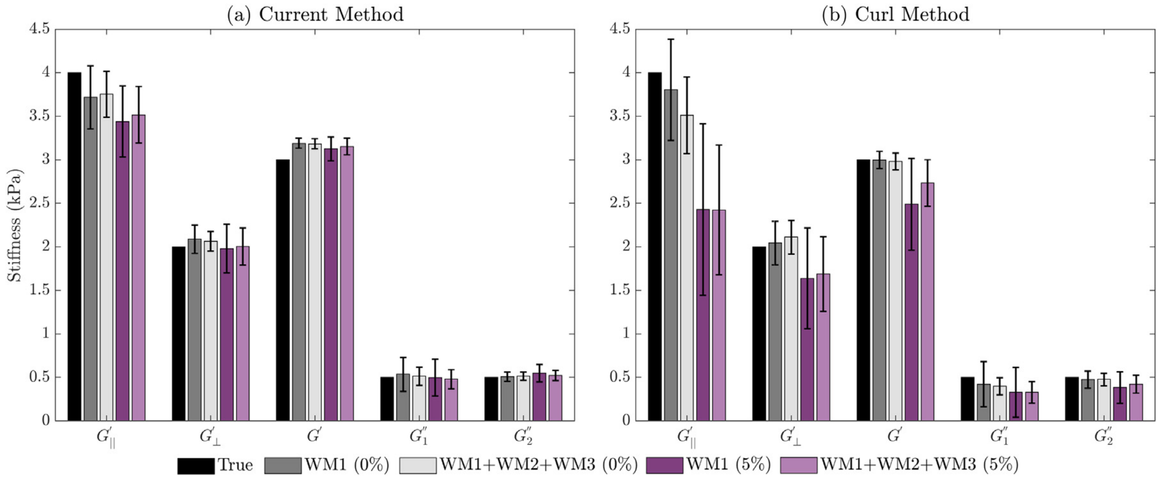

Fig. 11. Comparison of the shear moduli against ground truth for FD4 using both the (a) current and (b) curl methods. Results depict mean ± one standard deviation for WM1 with no noise (0%), WM1+WM2+WM3 with no noise (0%), WM1 with 5% noise added to the wave data and WM1+WM2+WM3 with 5% noise added to the wave data.

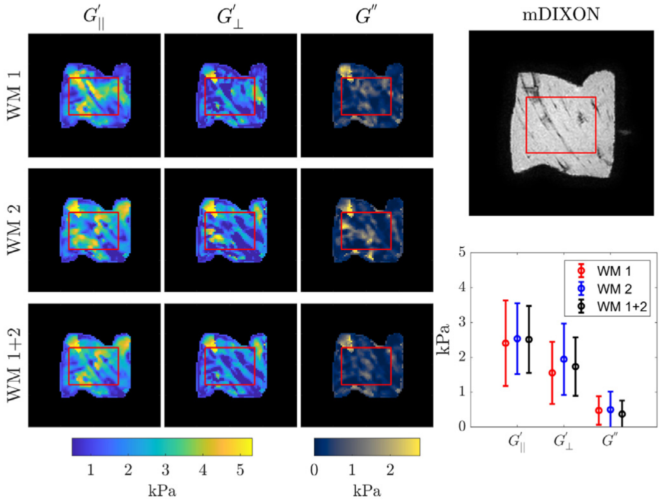

Fig. 12. Results from *ex vivo* muscle sample with both single and dual wave mode reconstruction for WM 1, 2 and 1+2. Left panel shows the shear modulus maps for each wave mode. The anatomical image (mDixon) is shown in the upper right panel. Group data for the ROI indicated in red on the images is shown in the bottom right panel (mean ± SD. The regions near the probes were excluded to minimise the effects of tissue compression where the probes contact the sample.

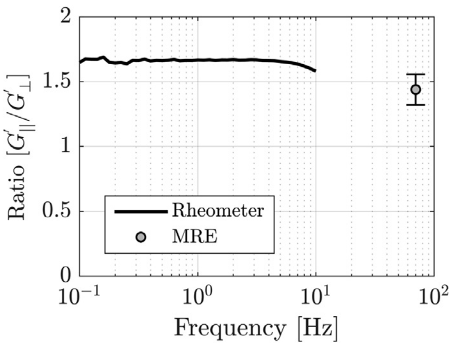

Fig. 13. A comparison between the anisotropic ratio ($G'_{||}/G'_{\perp}$) of the reconstructed stiffness estimates and the estimates from the eccentric rheometry. The anisotropic ratio from the rheometry measures (solid line) is estimated from the sample average $G'_{||}$ and $G'_{\perp}$, grouping both the results from para 1 and 2. The MRE results are expressed as the mean±SD of the three reconstructed estimates. From 4-10 Hz, inertial effects begin to influence the data, reflected as a decrease in the anisotropic ratio.

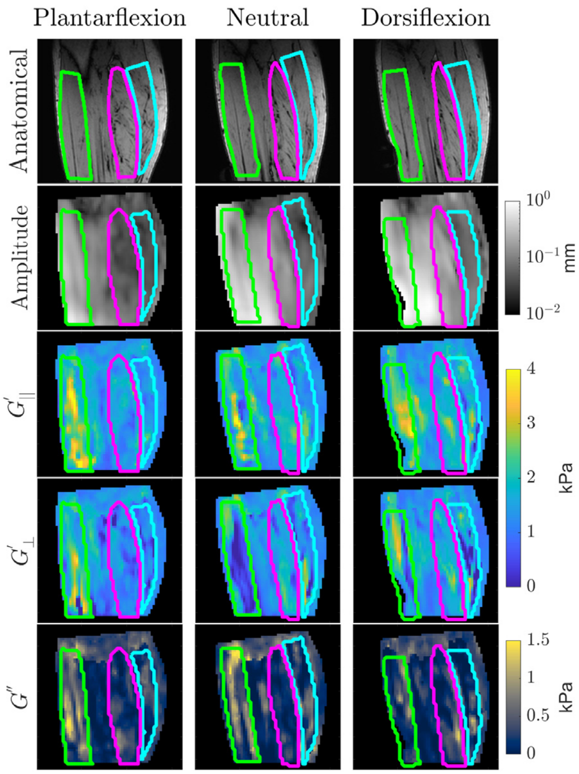

Fig. 14. Reconstructed stiffness maps for a representative subject with the ankle either in a plantarflexed, neutral or dorsiflexed position. The first row shows the mDixon out-of-phase anatomical image. The next row shows the shear wave amplitude, followed by estimated parallel and perpendicular stiffness, and, lastly, the loss modulus. The shear wave amplitude is displayed on a logarithmic scale, whereas all of the stiffness maps are linearly scaled. On all images, the ROIs of the TA (green), SOL (pink) and MG (blue) are highlighted.

3.3. *In vivo results*

Fig. 14 shows the reconstructed stiffness maps for a representative subject with the ankle in the plantarflexed, neutral and dorsiflexed positions. The TA is stretched during plantarflexion and slack during dorsiflexion. The measured shear moduli reflect this as an increased stiffness in plantarflexion compared to dorsiflexion. Conversely, the MG and SOL appear to increase in stiffness during dorsiflexion, as they are stretched. Fig. 15 shows the group data

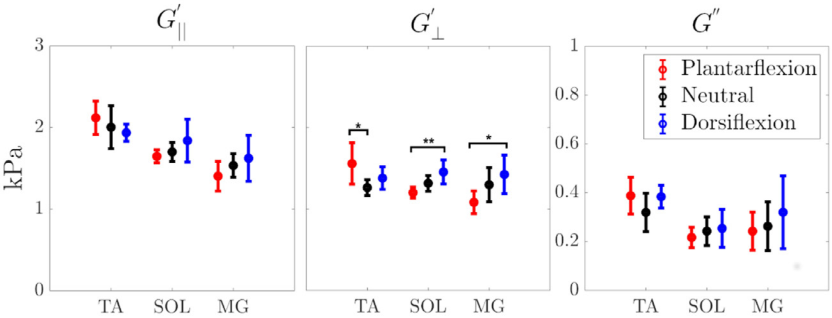

Fig. 15. Mean stiffness and 95% confidence intervals for the group estimated stiffness of the TA, SOL and MG muscles with the ankle in either a plantarflexed (red), neutral (black) or dorsiflexed (blue) position. From left to right, plots show $G'_{\parallel}$, $G'_{\perp}$ and G''. Significant comparisons are marked with an asterisk (*P < 0.05; **P <0.01).

(mean ± SD) highlighting the difference in muscle stiffness given the position of the ankle. On average, the transverse shear modulus ($G'_{\perp}$) was stiffer in the TA during plantarflexion than while in a neutral position (ANOVA, $\Delta G'_{\perp} = 0.29$kPa, P = 0.033), whereas, in the SOL (ANOVA, $\Delta G'_{\perp} = 0.25$kPa, P = 0.007) and MG (ANOVA, $\Delta G'_{\perp} = 0.34$kPa, P = 0.03), the transverse shear modulus ($G'_{\perp}$) was stiffer during dorsiflexion than in plantarflexion.

4. Discussion

In this study, we have developed a novel finite element based anisotropic inversion method, and an analysis pipeline that utilises displacements measured from MRE images along with fibre directions from DTI to calculate transversely isotropic linearly viscoelastic shear moduli. Using a combination of *in silico* tests and experimental data from *ex vivo* muscle tissue, we have demonstrated that the method accurately estimates the mechanical properties of anisotropic materials with minimal bias in the presence of typical levels of experimental noise in both displacement and fibre direction. With large levels of noise in the fibre direction, the method underestimates the degree of anisotropy, illustrating the importance of accurate diffusion tensor imaging. In the presence of large amounts of noise in the wave displacement data, the reconstruction method still produced adequate estimates of G'' and $G'_{\perp}$. We have also shown that the variability of parameter estimates decreases when using data from more than one input vibration source. This conclusion is consistent with previous suggestions (Tweten et al., 2017) that successful anisotropic MRE characterisation requires input data that captures wave propagation along and across dominant fibre directions within a tissue. We have also demonstrated that this method can be applied *in vivo* to human leg muscles, and is sensitive to increases in muscle tension due to leg flexion. This method is promising for the evaluation of anisotropic tissues *in vivo*, such as muscle and white matter.

4.1. Implications of results for MRE measurements

Overall, there was minimal bias in the shear moduli calculated from the *in silico* experiments and was more accurate in the presence of noise than the previous curl-based reconstruction method. Variability in estimates was improved further by including multiple wave modes. However, without noise, the simplest fibre field resulted in an underestimation of $G'_{\parallel}$ by 5% and an overestimation of $G'_{\perp}$ by 12%. This bias can partly be attributed to a lack of mode conversion of pushing loads applied on the boundaries of the cube into shear waves within the anisotropic portion. Fig. 8 illustrates that, for FD2, applying a shear load (WM6) in combination with a pushing load (WM3) results in the most accurate estimate of $G'_{\perp}$ (2% error). Therefore, efforts to increase the amount of shear waves in the anisotropic region may improve overall accuracy of the reconstruction method. Additionally, the accuracy depends on the complexity of the fibre field in the anisotropic region (Fig. 1). Rapidly varying fibre orientations introduced a degree of bias into the stiffness estimates, underestimating $G'_{\parallel}$. However, fibre orientations within unipennate skeletal muscles generally vary smoothly within a muscle, similar to FD1 - FD2. In bipennate muscles, there are two subregions with different directions, but within each subregion, the orientations are similar, analogous to FD3. However, the technique may be less accurate in structures with rapidly changing fibre directions, such as in regions of the brain or the tongue. The *in silico* experiments showed that the addition of noise in the wave data resulted in an underestimation of $G'_{\parallel}$ whereas $G'_{\perp}$ and G'' values were largely unaffected. When increasing noise was introduced into the fibre orientation, $G'_{\parallel}$ decreased whereas $G'_{\perp}$ increased. Therefore, with increasing disarray in the fibre orientation measurement, the reconstruction estimated $G'_{\parallel}$ and $G'_{\perp}$ as increasingly closer to the mean between their true values.

4.2. Comparison to other anisotropic reconstruction methods

Although *in silico* experiments illustrated a bias towards underestimating $G'_{\parallel}$ in the presence of noise, the bias was less pronounced with this new reconstruction method than a previous method (Qin et al., 2013a). This is further illustrated in utilising various fibre distributions and noise combinations. Additionally, with the proposed method, stiffness estimates were stable up to 5% noise in the wave displacements.

One advantage of this reconstruction method over previous methods is that it does not require directional filtering of the wave data to isolate waves travelling in the fibre direction (Manduca et al., 2003; Tweten et al., 2015; Kalra et al., 2019). Directional filtering requires choosing a discrete number of spatial filtering directions in order to isolate the wave components travelling in a preferred direction. This method utilises all wave data, thus bypassing a potential source of bias induced by manual selection of filter orientations. Other methods have also relied on application of the curl (Guo et al., 2015) to isolate the shear components of the wave motion, which require high order derivatives of potentially noisy data. This can induce bias in estimated stiffness values. The method presented in this paper, on the other hand, uses divergence-free test functions to eliminate the longitudinal wave component from the wave displacements.

Additionally, this method incorporates material orientations obtained directly from diffusion tensor images rather than an assumed material orientation (Guo et al., 2015; Schmidt et al., 2018). Two previous studies have investigated skeletal muscle stiffness in the medial gastrocnemius, soleus and tibialis anterior (Green et al., 2013; Guo et al., 2015) using MR elastography. Our results are consistent with Green et al. (2013), who found significant differences

Table 2
Mean lower leg muscle MRE stiffness estimates from two previous studies and the current study, acquired while the leg was in a neutral position (Fig. 15)

	TA		SOL		MG		
	$G'_\perp$	$G'_\parallel$	$G'_\perp$	$G'_\parallel$	$G'_\perp$	$G'_\parallel$	Freq.
Green et al.	0.66	0.78	0.65	0.83	0.66	0.86	60 Hz
Guo et al.	1.26	1.27	1.06	1.33	0.90	1.30	30-60 Hz
Current	1.26	2.00	1.32	1.70	1.30	1.53	50 Hz

between $G'_\perp$ and $G'_\parallel$ in the same three muscles of the lower leg in a neutral position. Muscle stiffness estimates from Guo et al. were derived using a multi-frequency estimation method and a different constitutive law with six unknown parameters ($G'_\perp$, $G'_\parallel$, $E'_\parallel$, $G''_\perp$, $G''_\parallel$, $E''_\parallel$). Additionally, DTI was not used to measure fibre orientations which may also account for differences in stiffness estimates. In general, the current study estimated higher stiffness values and greater anistropy in the TA than the previous two (Table 2). It was shown through the *in silico* experimental results that the previous curl-based method, used in Green et al. (2013) underestimated the stiffness in the presence of noise more so than the current method, which could account for the higher stiffness values in the current study.

In silico experiments allow for validation of reconstruction methods in a controlled way where the ground truth stiffness values are known. Previous studies have developed *in silico* tests which model viscoelastic (Zvietcovich et al., 2019) as well as anisotropic behaviour of tissues such as the brain (McGarry et al., 2021), skeletal muscle (Tweten et al., 2015; 2017; Hollis et al., 2017) and myocardium (Miller et al., 2018) with the aim of replicating *in vivo* wave patterns. McGarry et al. (2021) developed a person-specific finite element model of MRE wave propagation based on experimental data which was used to demonstrate errors in estimated stiffness when utilising isotropic reconstruction techniques. The tests developed in this study were not designed to represent any particular physiological structure and thus, were not compared with *in vivo* wave patterns. Previous *in silico* studies have modelled tissue as nearly incompressible with a defined bulk modulus or Poisson's ratio (e.g. McGarry et al. (2021); Tweten et al. (2017)) whereas an incompressible formulation was used in this analysis.

Another distinct difference between this and other anisotropic reconstruction methods is that this method describes the material using two shear moduli only whereas previous studies have often used three independent parameters to describe a nearly incompressible transversely isotropic material, including two shear moduli and a parameter representing the tensile anisotropy. Compared to methods which filter the displacements into slow and fast shear waves (e.g. Schmidt et al. (2018)), this study implies the existence of only a slow shear wave component whose speed varies with direction. Although this assumption may fail to detect material changes which solely impact tensile properties, the estimation of a parameter describing tensile anisotropy has been shown to be extremely sensitive to noise and requires complex and multiple wave fields (Tweten et al., 2017; Miller et al., 2018), which may be infeasible to acquire in a clinical setting. Conversely, the estimation of shear properties is more robust and may yet provide a means to assess changes in tissue structure due to physiological or pathological processes (Qin et al., 2014).

4.3. Assessment of reconstructed experimental data

We observed greater variability in shear moduli estimates in the *in vivo* and *ex vivo* MRE data than in the rheometry or *in silico* results. This likely reflects the combined effects of imaging-related noise and intra-muscle mechanical heterogeneity. The *in silico* mechanical parameters were inherently uniform within the different regions and, in the samples used for rheometry, connective tissues and blood vessels were excluded. This was not possible for the MRE experiments. This resulted in an underestimation of the $G'_\parallel$, and increased variation in the estimated parameters, similar to that demonstrated with the *in silico* tests with complex fibre distributions (Fig.s 6 and 12). The influence of different tissues within the sample is representative of the partial volume effect seen with the *in vivo* data, where the reconstructed parameters show greater variation than seen with the *in silico* testing (Fig. 14).

4.4. Application for studying tissue pathologies

There is considerable potential for the use of MRE to identify and track soft tissue pathologies, as has been demonstrated in the clinical use of MRE for tracking liver fibrosis. The *in vivo* experiments demonstrated that this new robust approach can detect changes in stiffness due to passive muscle stretching (Fig. 15). This may be used to enhance functional tests and enable the detection of tissue pathologies in anisotropic soft tissues *in vivo*. Specifically, this technique could enhance detection of disorders that primarily affect longitudinal fibres, and thus the mechanical behaviour along the fibre direction. In muscles, this could include dystrophic disorders e.g. Qin et al. (2014). In contrast, fatty infiltration may affect both parallel and perpendicular shear moduli. Neurodegenerative disorders are expected to preferentially alter neural tissue properties along the axonal fibre direction, such as along white matter tracts, and this technique could be used to detect and track such changes. Similarly, demyelinating disorders, while leaving the axons intact, may act to reduce the anisotropy of highly aligned white matter tracts, as the protective myelin sheath degenerates. The capacity of this technique to detect such effects should be explored in future studies. As the results from this study show, careful attention to the experimental processes are required to ensure that noise in both the wave data and tissue fibre orientations are minimised, as high noise tends to result in lower measured anisotropy. The additional accuracy gained by using multiple wave inputs will need to be balanced against the costs of additional scan time and practical considerations. For example, due to anatomical limitations, the potential for multiple wave input directions to the brain is limited. Care must also be taken in tissues with rapidly changing fibre orientations where this algorithm may also underestimate the anisotropy. Note, however, that this new method outperforms the older curl-based method (Qin et al., 2013; Sinkus et al., 2005) in the presence of noise.

4.5. Study limitations

The current study presents a new anisotropic reconstruction technique, demonstrates its strengths and limitations through a systematic analysis of *in silico* experiments, and applies it to both *ex vivo* and *in vivo* MRE data. In the current work, evaluation of fibre field variation, stiffness variation, viscosity, wave motions and uncertainties *in silico* were all tested in a simple example. This design was intentional, allowing for straightforward interpretation of each of these factors; however, more complex *in silico* cases could provide additional insight for specific applications (e.g. McGarry et al. (2021)). Further, while we extended our divergence-free FEM reconstruction from Fovargue et al. (2018a) to consider transversely isotropic materials (with an isotropic loss modulus) which broadens the approach to a new class of materials, its efficacy for more complex materials remains to be demonstrated. That said, the formulation presented enables substitution with other material models and should be straightforward to apply for other constitutive equations (especially those with a linear parameter dependence). The current analysis shows that estimated parameters are less accurate when the variation of material structure occurs too rapidly in space and in highly noisy data. However, both are improved over the previous curl-based approach (Sinkus et al., 2005; Qin et al., 2013a). The reliable application of these techniques *in vivo* requires the ability to synthesize multiple imaging modalities simultaneously, requiring image registration techniques (Klein et al., 2010). Further, acquisition of structure through imaging, such as DTI, can be slow and be subject to EPI distortions. However, acquisition times can be decreased for tissues with simpler microstructure and distortions corrected using a combination of affine and nonlinear registration steps, further extending the approach used here (Klein et al., 2010; Rueckert and Schnabel, 2010).

5. Conclusion

In this study, we have developed and validated a novel, numerically robust, transversely anisotropic MR elastography reconstruction method that combines information about tissue fibre structure and shear wave propagation characteristics to estimate linear viscoelastic shear moduli in the fibre direction and perpendicular to it, using a finite element based approach. Moreover, we have shown that this novel method reliably reproduces both the elastic and viscous shear moduli in the presence of realistic levels of noise in both the wave data and fibre orientation inputs. This represents a major step forward in overcoming limitations of existing anisotropic elastography reconstruction approaches. In addition, we have developed an image processing pipeline to enable the use of this reconstruction method that co-registers anatomical, MRE and diffusion tensor images, extracts fibre orientations from the DTI data, and then incorporates this into the reconstruction algorithm. The algorithm and image processing pipeline have been used to measure the anisotropic shear moduli of *ex vivo* skeletal muscles and lower leg muscles of human volunteers. In the latter case, it was shown that the method could detect changes in stiffness due to passive muscle stretching, indicating that the method is sensitive to changes in anisotropic tissue mechanics. This new reconstruction method can be used to quantify tissue mechanical properties of anisotropic soft tissues, such as muscle and white matter tracts, in health and disease.

Declaration of Competing Interest

The authors declare that they have no known competing financial interests or personal relationships that could have appeared to influence the work reported in this paper.

CRediT authorship contribution statement

Behzad Babaei: Conceptualization, Methodology. **Daniel Fovargue:** Methodology, Software, Validation. **Robert A. Lloyd:** Formal analysis, Investigation, Writing – original draft. **Renee Miller:** Software, Formal analysis, Writing – original draft. **Lauriane Jugé:** Investigation. **Max Kaplan:** Investigation. **Ralph Sinkus:** Writing – review & editing. **David A. Nordsletten:** Conceptualization, Methodology, Writing – original draft, Supervision. **Lynne E. Bilston:** Conceptualization, Investigation, Writing – original draft, Supervision.

Acknowledgments

This research was supported by a Discovery grant from the Australian Research Council (DP160100061). L.E.B. is supported by senior research fellowships from the National Health and Medical Research Council of Australia (APP1077934, APP1172988). D.N. would like to acknowledge funding from Engineering and Physical Sciences Research Council (EP/N011554/1 and EP/R003866/1).

Supplementary material

Supplementary material associated with this article can be found, in the online version, at doi:10.1016/j.media.2021.102212.

References

Anderson, A.T., Van Houten, E.E.W., McGarry, M.D.J., Paulsen, K.D., Holtrop, J.L., Sutton, B.P., Georgiadis, J.G., Johnson, C.L., 2016. Observation of direction-dependent mechanical properties in the human brain with multi-excitation MR elastography. Journal of the Mechanical Behavior of Biomedical Materials 59, 538–546.

Andersson, J.L., Skare, S., Ashburner, J., 2003. How to correct susceptibility distortions in spin-echo echo-planar images: application to diffusion tensor imaging. Neuroimage 20 (2), 870–888.

Bayly, P., Taber, L., Kroenke, C., 2014. Mechanical forces in cerebral cortical folding: a review of measurements and models. Journal of the mechanical behavior of biomedical materials 29, 568–581.

Bensamoun, S.F., Glaser, K.J., Ringleb, S.I., Chen, Q., Ehman, R.L., An, K., 2008. Rapid magnetic resonance elastography of muscle using one-dimensional projection. Journal of Magnetic Resonance Imaging 27 (5), 1083–1088.

Bensamoun, S.F., Ringleb, S.I., Chen, Q.S., Ehman, R.L., An, K.N., Brennan, M., 2007. Thigh muscle stiffness assessed with magnetic resonance elastography in hyperthyroid patients before and after medical treatment. Journal of Magnetic Resonance Imaging 26 (3), 708–713.

Bilston, L.E., 2018. Soft tissue rheology and its implications for elastography: Challenges and opportunities. NMR Biomed 31 (10), e3832.

Bilston, L.E., 2019. Brain tissue mechanical properties. In: Biomechanics of the Brain. Springer, pp. 71–95.

Bilston, L.E., Bolsterlee, B., Nordez, A., Sinha, S., 2019. Contemporary image-based methods for measuring passive mechanical properties of skeletal muscles in vivo. J Appl Physiol (1985) 126 (5), 1454–1464.

Bilston, L.E., Tan, K., 2014. Measurement of passive skeletal muscle mechanical properties in vivo: Recent progress, clinical applications, and remaining challenges. Annals of Biomedical Engineering 1–13.

Bolsterlee, B., D'Souza, A., Gandevia, S.C., Herbert, R.D., 2017. How does passive lengthening change the architecture of the human medial gastrocnemius muscle? Journal of Applied Physiology 122 (4), 727–738.

Brown, E., Cheng, S., McKenzie, D., Butler, J., Gandevia, S., Bilston, L., 2014. Tongue stiffness is lower in patients with obstructive sleep apnea during wakefulness compared with matched control subjects. Sleep. (in press, accepted 19th October, 2014)

Capilnasiu, A., Hadjicharalambous, M., Fovargue, D., Patel, D., Holub, O., Bilston, L., Screen, H., Sinkus, R., Nordsletten, D., 2019. Magnetic resonance elastography in nonlinear viscoelastic materials under load. Biomechanics and modeling in mechanobiology 18 (1), 111–135.

Chakouch, M.K., Pouletaut, P., Charleux, F., Bensamoun, S.F., 2016. Viscoelastic shear properties of in vivo thigh muscles measured by MR elastography. Journal of Magnetic Resonance Imaging 43 (6), 1423–1433.

Chaudhuri, P.K., Low, B.C., Lim, C.T., 2018. Mechanobiology of tumor growth. Chem Rev 118 (14), 6499–6515.

Cheng, S., Clarke, E.C., Bilston, L.E., 2008. Rheological properties of the tissues of the central nervous system: A review. Medical Engineering and Physics 30 (10), 1318–1337.

Cheng, S., Gandevia, S., Green, M., Sinkus, R., Bilston, L., 2011. Viscoelastic properties of the tongue and soft palate using mr elastography. Journal of biomechanics 44 (3), 450–454.

Cirka, H.A., Koehler, S.A., Farr, W.W., Billiar, K.L., 2012. Eccentric rheometry for viscoelastic characterization of small, soft, anisotropic, and irregularly shaped biopolymer gels and tissue biopsies. Annals of biomedical engineering 40 (8), 1654–1665.

Connesson, N., Clayton, E., Bayly, P., Pierron, F., 2015. Extension of the optimised virtual fields method to estimate viscoelastic material parameters from 3d dynamic displacement fields. Strain 51 (2), 110–134.

Feng, Y., Okamoto, R.J., Namani, R., Genin, G.M., Bayly, P.V., 2013. Measurements of mechanical anisotropy in brain tissue and implications for transversely isotropic material models of white matter. Journal of the Mechanical Behavior of Biomedical Materials 23, 117–132.

Fovargue, D., Fiorito, M., Capilnasiu, A., Nordsletten, D., Lee, J., Sinkus, R., 2020. Towards noninvasive estimation of tumour pressure by utilising mr elastography and nonlinear biomechanical models: a simulation and phantom study. Scientific reports 10 (1), 1–13.

Fovargue, D., Kozerke, S., Sinkus, R., Nordsletten, D., 2018. Robust mr elastography stiffness quantification using a localized divergence free finite element reconstruction. Medical image analysis 44, 126–142.

Fovargue, D., Nordsletten, D., Sinkus, R., 2018. Stiffness reconstruction methods for mr elastography. NMR in Biomedicine 31 (10), e3935.

Garcia, D., 2010. Robust smoothing of gridded data in one and higher dimensions with missing values. Computational statistics & data analysis 54 (4), 1167–1178.

Garcia, D., 2011. A fast all-in-one method for automated post-processing of piv data. Experiments in fluids 50 (5), 1247–1259.

Geng, G., Johnston, L.A., Yan, E., Britto, J.M., Smith, D.W., Walker, D.W., Egan, G.F., 2009. Biomechanisms for modelling cerebral cortical folding. Medical Image Analysis 13 (6), 920–930.

Gennisson, J.L., Deffieux, T., Fink, M., Tanter, M., 2013. Ultrasound elastography: principles and techniques. Diagn Interv Imaging 94 (5), 487–495.

Gennisson, J.-L., Deffieux, T., Macé, E., Montaldo, G., Fink, M., Tanter, M., 2010. Viscoelastic and anisotropic mechanical properties of in vivo muscle tissue assessed by supersonic shear imaging. Ultrasound in Medicine & Biology 36 (5), 789–801.

Gkretsi, V., Stylianopoulos, T., 2018. Cell adhesion and matrix stiffness: Coordinating cancer cell invasion and metastasis. Front Oncol 8, 145.

Green, M., Geng, G., Qin, E., Sinkus, R., Gandevia, S., Bilston, L., 2013. Measuring anisotropic muscle stiffness properties using elastography. NMR in Biomedicine 26 (11), 1387–1394.

Green, M. A., Bilston, L. E., van Houten, E., Sinkus, R.,. In-vivo brain viscoelastic anisotropic properties using dti and mr-elastography. In: Proc 17th ISMRM.

Guo, J., Hirsch, S., Scheel, M., Braun, J., Sack, I., 2015. Three-parameter shear wave inversion in MR elastography of incompressible transverse isotropic media: Application to in vivo lower leg muscles. Magnetic Resonance in Medicine 75 (4), 1537–1545.

Hollis, L., Barnhill, E., Perrins, M., Kennedy, P., Conlisk, N., Brown, C., Hoskins, P., Pankaj, P., Roberts, N., 2017. Finite element analysis to investigate variability of mr elastography in the human thigh. Magnetic resonance imaging 43, 27–36.

Honarvar, M., Rohling, R., Salcudean, S.E., 2016. A comparison of direct and iterative finite element inversion techniques in dynamic elastography. Physics in Medicine and Biology 61, 3026–3048.

Kalra, P., Raterman, B., Mo, X., Kolipaka, A., 2019. Magnetic resonance elastography of brain: Comparison between anisotropic and isotropic stiffness and its correlation to age. Magnetic Resonance in Medicine 82 (2), 671–679.

Klatt, D., Papazoglou, S., Braun, J., Sack, I., 2010. Viscoelasticity-based MR elastography of skeletal muscle. Physics in Medicine and Biology 55 (21), 6445–6459.

Klein, S., Staring, M., Murphy, K., Viergever, M.A., Pluim, J.P., 2010. elastix: a toolbox for intensity-based medical image registration. IEEE Trans Med Imaging 29 (1), 196–205.

Knutsson, H., Westin, C.F., Granlund, G., 1994. Local multiscale frequency and bandwidth estimation. In: Proceedings of 1st International Conference on Image Processing, 1, pp. 36–40.

Lee, J., Cookson, A., Roy, I., Kerfoot, E., Asner, L., Vigueras, G., Sochi, T., Deparis, S., Michler, C., Smith, N.P., Nordsletten, D., 2016. Multiphysics computational modeling in cheart. SIAM Journal on Scientific Computing 38 (3), C150–C178.

Llinares-Benadero, C., Borrell, V., 2019. Deconstructing cortical folding: genetic, cellular and mechanical determinants. Nature Reviews Neuroscience 20 (3), 161–176.

Malvern, L.E., 1969. Introduction to the Mechanics of a Continuous Medium.

Manduca, A., Lake, D.S., Kruse, S.A., Ehman, R.L., 2003. Spatio-temporal directional filtering for improved inversion of MR elastography images. Medical Image Analysis 7 (4), 465–473.

Manjón, J.V., Coupé, P., Concha, L., Buades, A., Collins, D.L., Robles, M., 2013. Diffusion weighted image denoising using overcomplete local pca. PLOS ONE 8 (9), e73021.

McGarry, M., Houten, E.V., Guertler, C., Okamoto, R., Smith, D., Sowinski, D., Johnson, C., Bayly, P., Weaver, J., Paulsen, K., 2021. A heterogenous, time harmonic, nearly incompressible transverse isotropic finite element brain simulation platform for MR elastography. Physics in Medicine and Biology 66 (5).

Miller, R., Kolipaka, A., Nash, M.P., Young, A.A., 2018. Estimation of transversely isotropic material properties from magnetic resonance elastography using the optimised virtual fields method. International Journal for Numerical Methods in Biomedical Engineering 34 (6), e2979.

Muthupillai, R., Lomas, D., Rossman, P., Greenleaf, J., Manduca, A., Ehman, R., 1995. Magnetic resonance elastography by direct visualization of propagating acoustic strain waves. Science 269 (5232), 1854–1857.

Namani, R., Wood, M.D., Sakiyama-Elbert, S.E., Bayly, P.V., 2009. Anisotropic mechanical properties of magnetically aligned fibrin gels measured by magnetic resonance elastography. J Biomech 42 (13), 2047–2053.

Nicolle, S., Palierne, J.F., 2010. Dehydration effect on the mechanical behaviour of biological soft tissues: Observations on kidney tissues. Journal of the Mechanical Behavior of Biomedical Materials 3 (8), 630–635.

Novak, C., Horst, E., Mehta, G., 2018. Review: Mechanotransduction in ovarian cancer: Shearing into the unknown. APL Bioeng 2 (3), 031701.

Okamoto, R.J., Clayton, E.H., Bayly, P.V., 2011. Viscoelastic properties of soft gels: comparison of magnetic resonance elastography and dynamic shear testing in the shear wave regime. Physics in Medicine and Biology 56 (19), 6379–6400.

Qin, E.C., Jugé, L., Lambert, S.A., Paradis, V., Sinkus, R., Bilston, L.E., 2014. In vivo anisotropic mechanical properties of dystrophic skeletal muscles measured by anisotropic mr elastographic imaging: the mdx mouse model of muscular dystrophy. Radiology 273 (3), 726–735.

Qin, E.C., Sinkus, R., Geng, G., Cheng, S., Green, M., Rae, C.D., Bilston, L.E., 2013. Combining mr elastography and diffusion tensor imaging for the assessment of anisotropic mechanical properties: a phantom study. Journal of Magnetic Resonance Imaging 37 (1), 217–226.

Qin, E.C., Sinkus, R., Geng, G., Cheng, S., Green, M., Rae, C.D., Bilston, L.E., 2013. Combining mr elastography and diffusion tensor imaging for the assessment of anisotropic mechanical properties: A phantom study. Journal of Magnetic Resonance Imaging 37 (1), 217–226.

Romano, A., Scheel, M., Hirsch, S., Braun, J., Sack, I., 2012. In vivo waveguide elastography of white matter tracts in the human brain. Magnetic Resonance in Medicine 68 (5), 1410–1422.

Romano, A.J., Shirron, J.J., Bucaro, J.A., 1998. On the noninvasive determination of material parameters from a knowledge of elastic displacements theory and numerical simulation. IEEE Trans. Ultrason. Ferroelectr. Freq. Control 45 (3), 751–759.

Rueckert, D., Schnabel, J.A., 2010. Medical image registration. In: Biomedical image processing. Springer, pp. 131–154.

Schmidt, J., Tweten, D., Badachhape, A., Reiter, A., Okamoto, R., Garbow, J., Bayly, P., 2018. Measurement of anisotropic mechanical properties in porcine brain white matter ex vivo using magnetic resonance elastography. Journal of the Mechanical Behavior of Biomedical Materials 79, 30–37.

Sigrist, R.M.S., Liau, J., Kaffas, A.E., Chammas, M.C., Willmann, J.K., 2017. Ultrasound elastography: Review of techniques and clinical applications. Theranostics 7 (5), 1303–1329.

Sinkus, R., Lorenzen, J., Schrader, D., Lorenzen, M., Dargatz, M., Holz, D., 2000. High-resolution tensor mr elastography for breast tumour detection. Physics in Medicine & Biology. 45 (6), 1649–1664.

Sinkus, R., Tanter, M., Catheline, S., Lorenzen, J., Kuhl, C., Sondermann, E., Fink, M., 2005. Imaging anisotropic and viscous properties of breast tissue by magnetic resonance-elastography. Magnetic resonance in medicine 53 (2), 372–387.

Smith, D.R., Guertler, C.A., Okamoto, R.J., Romano, A.J., Bayly, P.V., Johnson, C.L., 2020. Multi-excitation magnetic resonance elastography of the brain: Wave propagation in anisotropic white matter. Journal of Biomechanical Engineering 142 (7).

Takaza, M., Moerman, K.M., Gindre, J., Lyons, G., Simms, C.K., 2013. The anisotropic mechanical behaviour of passive skeletal muscle tissue subjected to large tensile strain. Journal of the mechanical behavior of biomedical materials 17, 209–220.

Tan, K., Cheng, S., Juge, L., Bilston, L.E., 2015. Characterising skeletal muscle under large strain using eccentric and fourier transform-rheology. J Biomech 48 (14), 3788–3795.

Tweten, D., Okamoto, R., Bayly, P., 2017. Requirements for accurate estimation of anisotropic material parameters by magnetic resonance elastography: A computational study. Magnetic Resonance in Medicine 78 (6), 2360–2372.

Tweten, D.J., Okamoto, R.J., Schmidt, J.L., Garbow, J.R., Bayly, P.V., 2015. Estimation of material parameters from slow and fast shear waves in an incompressible, transversely isotropic material. Journal of Biomechanics 48 (15), 4002–4009.

Van Houten, E.E., Miga, M.I., Weaver, J.B., Kennedy, F.E., Paulsen, K.D., 2001. Three-dimensional subzone-based reconstruction algorithm for MR elastography. Magn. Reson. Med. 45, 827–837.

Wang, S., Larin, K.V., 2015. Optical coherence elastography for tissue characterization: a review. J Biophotonics 8 (4), 279–302.

Yeh, F.-C., Verstynen, T.D., Wang, Y., Fernández-Miranda, J.C., Tseng, W.-Y.I., 2013. Deterministic diffusion fiber tracking improved by quantitative anisotropy. PLOS ONE 8 (11). e80713

Zvietcovich, F., Baddour, N., Rolland, J.P., Parker, K.J., 2019. Shear wave propagation in viscoelastic media: Validation of an approximate forward model. Physics in Medicine and Biology 64 (2).